Study of Preamplification Circuits for Micromegas Detectors

Studie von Vorverstärker-Schaltkreisen für Micromegas Detektoren

Masterarbeit an der Fakultät für Physik
der
Ludwig-Maximilians-Universität München

vorgelegt von
Quirin Steinbacher
geboren in Tegernsee

München, den 06.05.2016

Gutachter: Prof. Dr. Otmar Biebel

Kurzfassung

Micromegas-Detektoren sind Gas betriebene Teilchen-Detektoren. Sie können Teilchen über deren Ionisationsprozess im aktiven Gas-Volumen des Detektors aufspüren und erlauben des Weiteren Rückschlüsse über deren Trajektorie. Sie bestechen durch ihre einfache und kostengünstige Konstruktionsweise und ermöglichen die Detektion von Teilchen mit einer hohen Ortsauflösung und bei hohen Treffer-Raten.

Durch von außen einwirkende elektrische Felder, welche an die Auslesestreifen des Detektors koppeln, kommt es zu einer Verfälschung des Signals, dem so genannten Common-Mode-Noise. Hierbei überlagert sich das von außen kommende Signal mit dem Signal des Detektors.

Für die Auslese von Micromegas-Detektoren wird eine Auslese Elektronik bentigt. Fr diese Arbeit wird für die direkte Auslese der Streifen hauptsächlich der analoge APV (Analog Pipeline Voltage) Chip verwendet. Der APV Chip verarbeitet das Signal von bis zu 128 Streifen gleichzeitig und in analoger Weise. Das Signal jedes Kanals wird hierbei zuerst verstärkt und dann geformt. Hierbei kommt es aufgrund des Designs des APV Chips zu einer weiteren Verfälschung des Signals dem so genannten Baseline-Shift.

Nachdem das Signal auf der APV Karte zwischengespeichert wurde, wird es dann in analoger Form an die ADC (**A**nalogue **D**igital **C**onverter) Karte weiter gesandt, welches das Signal dann digitalisiert. Auch hierbei kommt es zu einer weiteren Verfälschung des ursprünglichen Signals.

Es wurden mit einem großem Micromegas Detektor in der Cosmic Ray Facility in Garching bei München sowie mit einem aus vier Micromegas Detektoren bestehenden Micromegas Teleskop am Tandem Beschleuniger ebenfalls in Garching bei München Daten genommen. Eine detaillierte Datenanalyse ermöglichte eine genaue Untersuchung der oben genannten Signalstörung.

Es wurden Algorithmen zur Korrektur der Signaldaten entwickelt. Die Korrekturen konnten erfolgreich auf die Daten angewandt werden und eine Verbesserung der Winkelauflsung der Detektoren konnte dadurch erzielt werden.

Abstract

Micromegas detectors are gaseous particle detectors. They enable the detection of particles through their ionization processes inside the active gas volume of the detector and allow the reconstruction of the trajectory of the traversing particle. They are inexpensive in construction, have a high spatial resolution and are able to handle high hit rates.

Elctomagnetic fields from the outside of the detector can couple to the readout-strips. This leads to a signal distortion, also known as common mode noise. The noise signal is superimposed with the physical signal.

For the readout of micromegas detectors, readout electronics are needed. For the readout of the strips, the analog APV (Analog Pipeline Voltage) chip has been used. The APV processes the analog signals of 128 strips individually and simultaniously. The signal is first amplified and than shaped. The design of the APV chip leads to a signal distortion, the so called baseline shift.

After buffering the signal on the APV, it is sent to the ADC (**A**nalogue **D**igital **C**onverter) board, which digitizes the signals, as an analog pulse. Hereby, the signals are further biased.

Data was acquired with a large micromegas chamber at the cosmic ray facility in Garching, near Munich, and with a micromegas telescope at the Tandem accelerator, which is also located in Garching. A detailed analysis of the data allowed for a study of the distortions.

Methods for the correction of the data have been developed and tested on the acquired data. An improvement in angular resolution of the micromegas could be shown.

Contents

Chapter 1

The Micromegas Detector and the ATLAS Experiment

The LHC (**L**arge **H**adron **C**ollider) [5] is a synchrotron for proton-proton collision at the CERN (**C**onseil **E**uropéen pour la **R**echerche **N**ucléaire) located at the outskirts of Geneva, Switzerland. Protons are accelerated in two parallel beam pipes in opposite directions and then brought to collision with a center of mass energy of up to 13TeV, the luminosity of the experiment is about $10^{34} cm^{-2} s^{-1}$. The final accelerator ring is installed in a tunnel with a circumference of about 27 km. In four interactions points the beams are crossed and particles are brought to collision. Here, four large experiments ALICE, ATLAS, CMS and LHCb are installed [5].

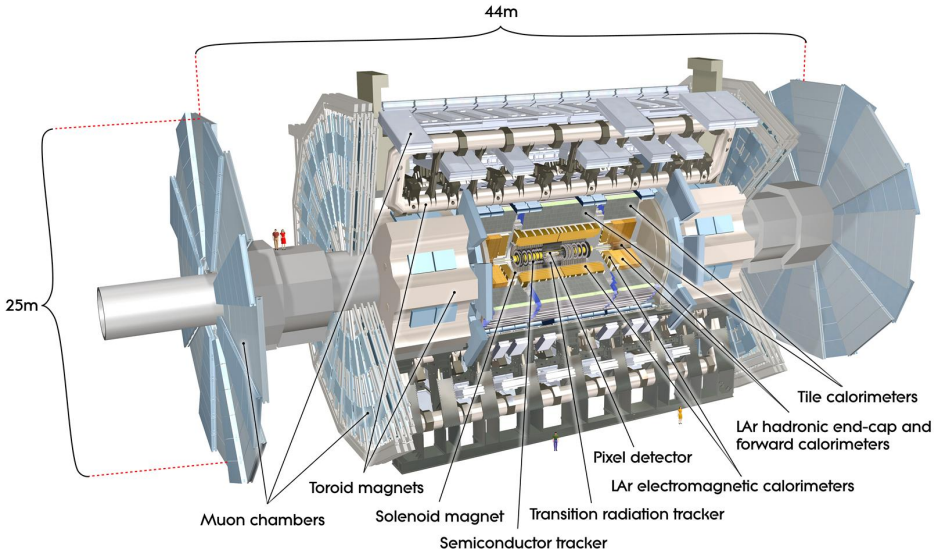

Figure 1.1: Cross section of the ATLAS detector showing the detector dimensions and the most important components. Taken from [2]

ATLAS (**A** **T**oroidal **L**HC **A**pparatu**S**), see Fig. 1.1, is a particle detector with an almost complete angular coverage. It can be divided in three concentric regions around the beam axis, the inner detector, the calorimeters and the muon spectrometer.

In 2018 another upgrade for ATLAS is scheduled to further improve luminosity. In this upgrade the monitored drift tubes chambers in the small wheel region will be replaced by small strip thin gap chambers and micromegas detectors, which can handle future hit rates. In part, these micromegas detectors will be produced at LMU Munich, for the test and calibration of these the readout-electronics which are studied in the context of this thesis will be used.

Chapter 2

The Micromegas Detector

2.1 Functional Principle

Micromegas (**M**icro **M**esh **G**aseous),proposed by Giomataris [9], are gaseous particle detectors used for the detection of ionizing particles. They are capable of high rate particle detection of up to 2GHz and have a high spatial resolution of about 50 μm [1]. Furthermore their components are inexpensive and they are relatively easy to build. Micromegas consist of a cathode, a stainless steel micro-mesh and an anode, see Fig. 2.1. The active gas volume of the detector between anode and cathode is divided into drift and amplification region. The drift region is located between cathode and micro-mesh and the amplification region between micro-mesh and anode.

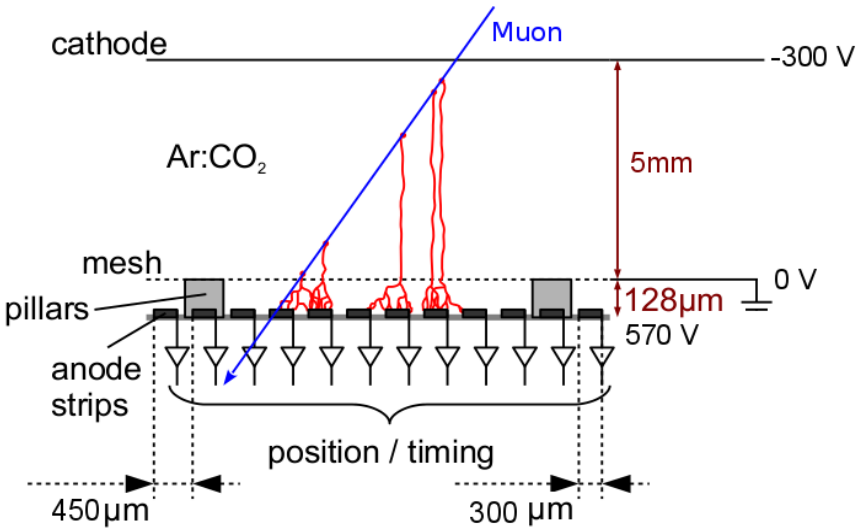

Figure 2.1: Schematic drawing of a micromegas detector, consisting of a cathode, a micro-mesh and an anode. The typical dimensions of micromegas built at our institute for the drift region, the amplification region and the strips are noted in this diagram. Taken from [1]

A traversing particle ionizes the gas mixture inside the detector. Electrons will then drift towards the micro-mesh and avalanche in the amplification region. Charge ac-

cumulates on the anode and the signal can then be read out from the capacitively readout-strips individually. The timing and charge information enable a reconstruction of the trajectory of the traversing particle.

2.2 Particle Interaction

As previously mentioned, particle interaction in form of ionization allows for the detection of traversing particles inside the active gas volume of the micromegas detector. The mean energy loss per path length of charged particles moving through matter due to excitation or ionization of atoms can be calculated via the Bethe-Bloch formula:

$$\langle \frac{dE}{dx} \rangle = -4\pi N_A r_e^2 m_e c^2 \rho \frac{Z z^2}{A\beta^2} \left(\frac{1}{2} ln \frac{2 m_e c^2 \beta^2 \gamma^2 T_{max}}{I^2} - \beta^2 - \frac{\delta}{2} \right) \tag{2.1}$$

The mean energy loss per path length $\langle \frac{dE}{dx} \rangle$ is expressed in terms of the Avogadro constant N_A, the classical electron radius r_e, the electron mass m_e, the speed of light c, the density of the material ρ, the atomic number of the material Z, the charge of the moving particle z, the atomic weight of the absorbing material A, $\beta = v/c$ where v is the speed of the particle and c the speed of light, $\gamma = (1-\beta^2)^{-\frac{1}{2}}$, the maximum energy transfer to a electron in a single collision $T_{max} \approx 2 m_e c^2 \beta^2 \gamma^2$, the mean excitation energy I and the density correction factor δ which can be found in [8].

For $Ar:CO_2$ with a ratio of 93:7 and $Ne:CF_4$ with a ratio of 80:20, which are typical gas mixtures used at LMU Munich, the mean energy loss per path length was calculated for a particle with an elementary charge and $\beta\gamma$ ranging from 0.1 to 2000, as shown in Fig. 2.2.

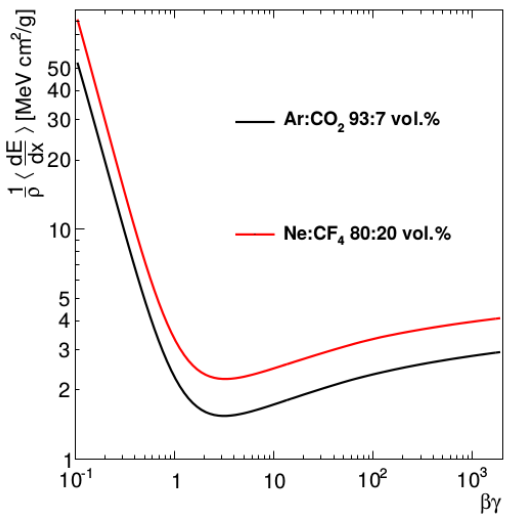

Figure 2.2: Energy loss of a particle with an elementary charge in $Ar:CO_2$ with a ratio of 80:20 and $Ne:CF_4$ with a ratio of 93:7 in dependency of $\beta\gamma$. Taken from [3]

2.3 Charge Carrier Drift and Amplification

It is important to consider the drift of ions inside the active gas volume of the detector as we want to suppress the recombination with electrons. The ions are drifting relatively slowly towards the cathode of the detector. Their mean drift velocity can be calculated using the following formula:

$$v_d = \mu E \frac{p_0}{p} \tag{2.2}$$

The drift velocity v_d is expressed in terms of the mobility μ, the electric field E, the nominal pressure p_0 and the gas pressure p. In the following table one can find the ion mobilities for $Ar:CO_2$ at a ratio 93:7 and $Ne:CF_4$ at a ratio of 80:20.

Gas	**Mobility [cm $V^{-1}s^{-1}$]**
Ar	1.54
CO_2	1.09
Ne	4.7

Table 2.1: Ion mobilities for the components of the gas mixtures $Ar:CO_2$ and $Ne:CF_4$, which are commonly used for micromegas.

The faster the ions reach the cathode, the fewer electrons recombine in the following events, as there are less ions left in the active gas volume. Therefore, a faster ion drift enables a higher rate of detection. As the mobility of Ne is about three times higher than the mobility of Ar $Ne:CF_4$ is preferred over $Ar:CO_2$ for high rate particle detection.

As electrons are at least a factor of 1000 lighter than ions, their drift in the presence of an electric field is a more complex process and quantum mechanical effects should be considered. The electron velocity strongly depends on the gas mixture in use. MAGBOLTZ [7] is a program which is used for the simulation of the drift velocity in dependence of the field strength. In the following Fig. 2.3 the electron drift velocity is plotted versus the field strength for $Ne:CF_4$ with a ratio of 80:20.

Little admixtures of H_2O to the $Ne:CF_4$ gas mixture, however, lower the electron drift velocity as can be seen in Fig. 2.4.

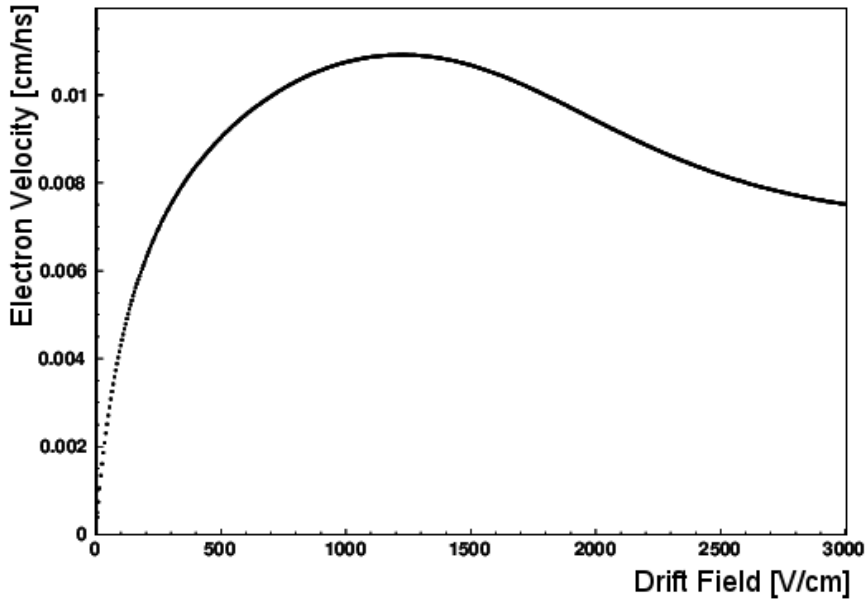

Figure 2.3: Electron drift velocity plotted versus the field strength for an $Ne{:}CF_4$ gas mixture with a ratio of 80:20.

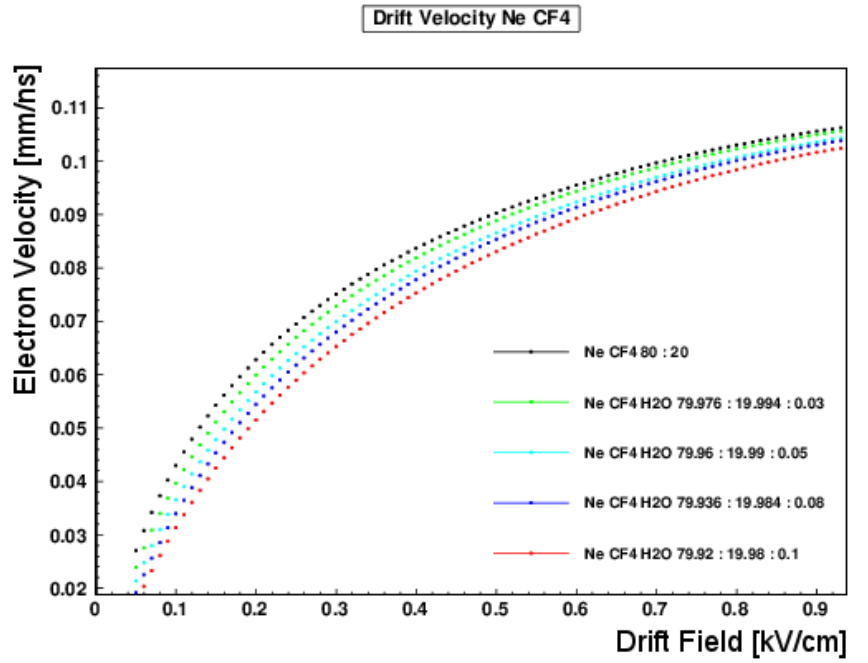

Figure 2.4: Electron drift velocity plotted for $Ne{:}CF_4$ with admixtures of H_2O. The ratios of the gas mixtures are noted in percent in the diagram.

During the measurements, the detectors are operated with a slight overpressure. This ensures that no substances from the outside enter the detector. For storage, however, the valves of the detectors were simply blocked, so that humidity could have entered the detector. Therefore an admixture of H_2O in the per mille range to the $Ne{:}CF_4$ gas mixture seems conceivable.

2.4 Discharge protection

The amplification field between micro-mesh and anode is on the order of kV/cm. This can lead to discharges in form of a conductive plasma in the amplification region, which are not destructive but cause dead time of the affected strips. The resistive and floating strip micromegas types were developed to reduce the dead time.

2.4.1 Resistive Strip Micromegas

The resistive strip micromegas type is characterized by the use of high resistivity anode-strips.

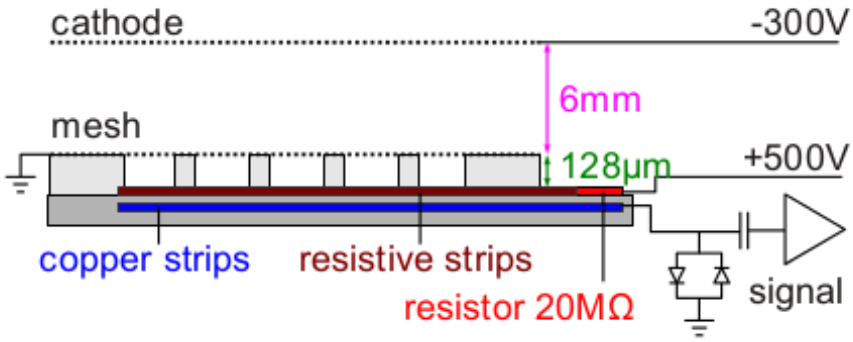

Figure 2.5: Resistive strip micromegas. Taken from [1]

The readout-strips are coupled capacitively to the resistive-strips while being separated from them by a layer of insulating material. The resistive-strips are connected to the HV power supply via high ohmic resistors. In case of discharges the resistive-strips are charged up only locally, such that the electric field in that region quickly reduces to zero interrupting the discharge. Because of their low capacitance, the recharge time is very low and the recharge does not affect the other strips. Resistive strip micromegas can be used for applications with hit rates up to $100kHz/cm^2$ [1].

2.4.2 Floating Strip Micromegas

The floating strip type is the most advanced discharge tolerant micromegas type.

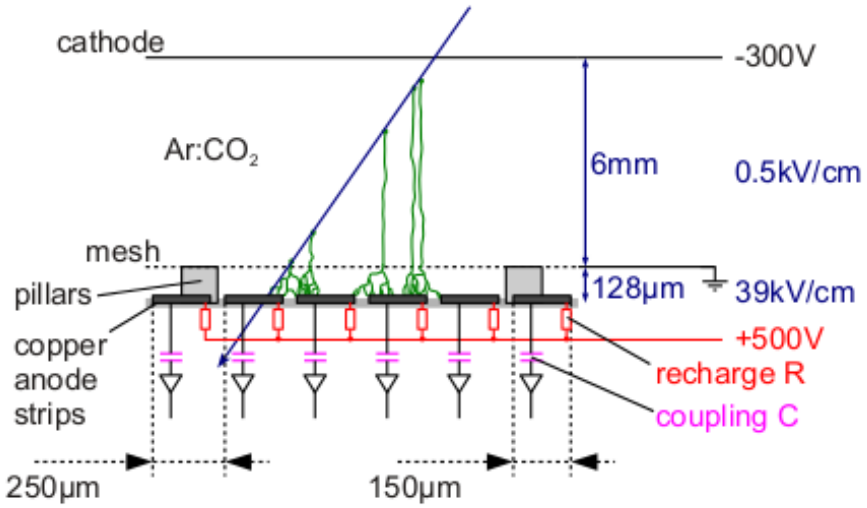

Figure 2.6: Floating strip micromegas. Taken from [1]

Its amplification region is formed by a micro-mesh and copper floating-strips. The floating-strips are individually connected to a high voltage power source via large resistors ($R \geq 20$ MΩ). In case of discharges the charge can "float" on the strips, such that the potential between floating-strips and mesh quickly levels out, disrupting the discharge. The strip capacitance is very small, this leads to very quick recharge times. The readout-strips are coupled to the floating-strips capacitively.

Chapter 3

Readout-Electronics

To transform the physical charge signal on the readout-strips into a data format which can be stored on a PC, readout-electronics are needed. In the following, the readout-electronics which have been used to acquire data in the context of this thesis will be described. An overview of a readout-system is given in Fig. 3.1. Here, the signal from the detector is first processed via an APV25 based front end board, which processes the analog signals. The signals are then sent via an HDMI cable to the ADC card, which digitizes the signals. The data is then merged by the FEC card and optionally a SRU before it is sent to the DAQ unit.

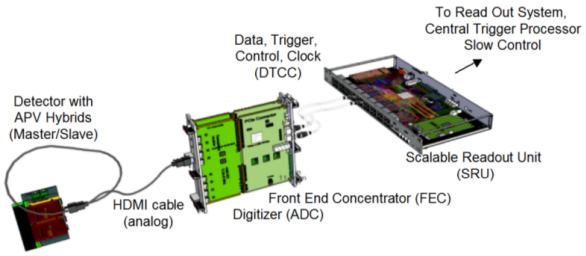

Figure 3.1: Scheme of a scaleable readout-system, taken from [10]

3.1 The APV25 front end board

APV25 (**A**nalog **P**ipeline **V**oltage Mode) based front end boards [4], see Fig. 3.2, are used to acquire time-resolved charge signals. They have been developed for the readout of silicon strip detectors in the CMS tracker.
The APV25 front end board is directly connected to the readout-strips of the micromegas detector via a 130 pin connector. The readout-strips are then capacitively coupled to the channels of the chip via high voltage capacitors. An additional circuit of fast diodes protects the APV25 chip from discharges. The APV chip can process signals of 128 readout-strips individually and simultaneously. Each channel of the APV chip has a preamplifier, a shaper and a 192 column deep analog storage ring. The APV board is powered with 5V over an HDMI cable from the ADC/FEC board. The APV chip itself is equipped with the voltage controller. It is important to note that all pipelines are supplied by the same power source. This will lead to signal distortion

as we will see later. After processing, the signals are stored on the 192 column deep analog memory ring at the LHC frequency of 40MHz. Upon reception of a trigger signal, certain parts of the memory are marked for read out. The data is output by an FIR(APSP) (**F**inite **I**mpulse **R**esponse) filter, which transforms the stored data into 25ns pulses. Again, these pulses are temporarily stored in a buffer before they are sent to the ADC by a multiplexer.

The APV25 front end board comes in a master and a slave version. The difference between master and slave version in design is the HDMI plug and the 25PLL (**P**hase **L**ock **L**oop) chip, which only the master APV board possesses. Master and slave boards can be connected via a 16 pin flat ribbon cable and are used in pairs. The master APV board is then connected to the ADC via an HDMI cable. The signal output of the slave board via the master board biases the signal of the slave board, as we will see later.

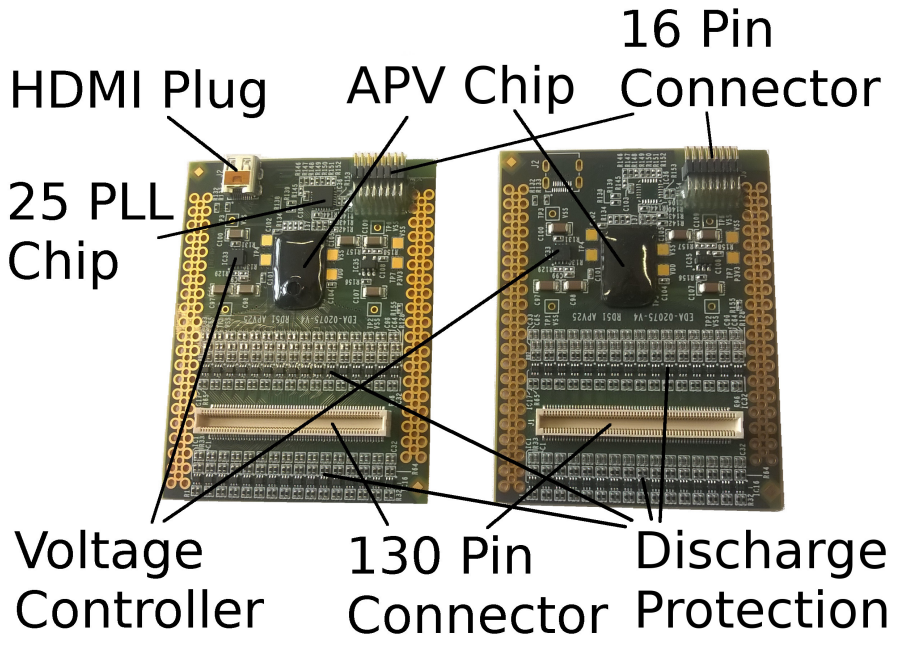

Figure 3.2: Picture of a master APV board on the left and a slave APV board on the right.

The design of the chip can be seen in Fig. 3.3. On the front end side, the 128 pads for the input of the readout-strips are arranged in two rows: The even numbered pads are on the outside while the odd numbered pads are on the inside. GND pads are located in the middle for the power supply of the preamplifier and shaper stages. The different length of the electric contacts of the GND pads to the pipelines is the only difference in the power supply of the pipelines. the pads for the readout of the memory, the clock, the trigger and the power supply are located on the back end.

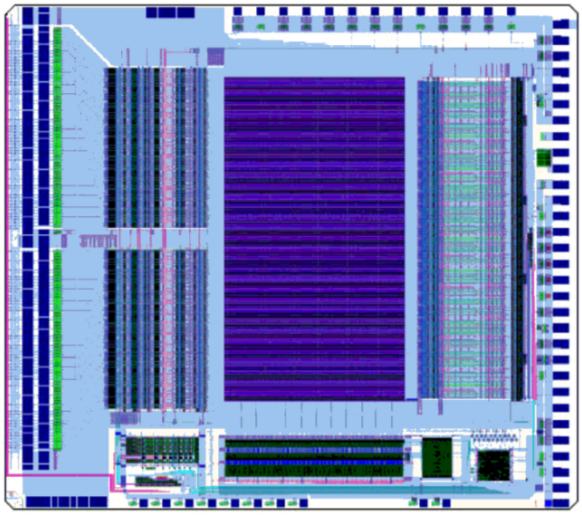

Figure 3.3: Design of the APV Chip. Taken from [4]

For the further context of this thesis, it is important to understand the assignment of strip number, channel number and sending number to each readout-strip. The strip number is assigned to each strip according to its position inside the detector and the channel number is assigned to each strip according to its channel position on the APV chip, as seen in Fig. 3.4. The relation between strip number and channel number can best be seen at the connection point of the readout-strips and the APV board. The two sides of the 130 pin connector can be divided into even and odd channel numbers.

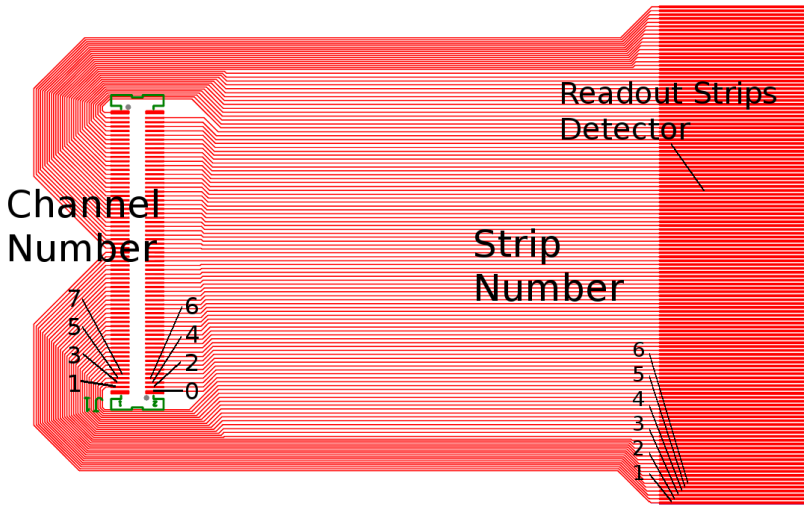

Figure 3.4: Section of the readout-board design.

The charge values of the strips are sent to the ADC by the multiplexer. The sending order is related to the channel number via the following relation:

$$n_{ch} = 32 * (j \, MOD \, 4) + 8 * int(j/4) - 31 * int(j/16) \tag{3.1}$$

Relation of the channel number n_{ch} to the sending number j, where MOD stands for the modulo operation and int stands for the integer cast in the C programming language.

The following table shows the output of channels by the APV in sending order, giving a relation between sending, channel and strip number.

Sending Number	Channel Number	Strip Number
0	0	33
1	32	49
2	64	65
3	96	81
4	8	37
5	40	53
6	72	69
7	104	85
8	16	41
9	48	57
10	80	73
11	112	89
12	24	45
⋮	⋮	⋮

Table 3.1: APV output in sending order.

Consecutive channels in sending number show distances of 32, 88 and 119 in channel numbers, how often those distances are counted for the output of one APV, can be seen in the following table.

Distance	Count
32	96
88	24
119	7

Table 3.2: Distances of consecutive channels in sending order.

3.2 Common Mode Noise

Electromagnetic signals from the outside of the detector can couple in identical manner to many readout-strips. The electric field will then force the electrons on the strip to move. This causes a charging and a discharging of the capacitors which connect the strips to the APV channels and therefore a variation of charge on the strips is detected by the APV chip. The noise signal is superposed with the real physical signal.

3.3 Baseline Shift

As previously mentioned, all pipelines of the APV chip are supplied with power by the same source, see Fig. 3.5.

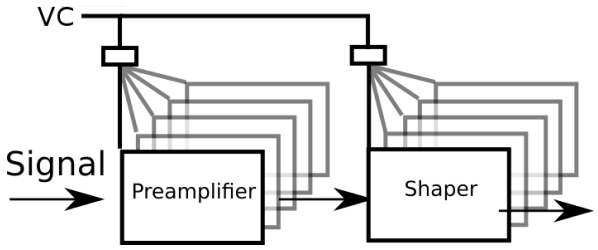

Figure 3.5: APV power distribution.

For a standard micromegas detector like the one shown in Fig. 2.1 more than three channels pick up a signal in case of a particle detection. The preamplifiers of the affected channels will then drain more power as the charge values on those channels rise. This leads to a very short voltage drop for all channels on the same APV, resulting in a lower signal on all channels on this APV.

3.4 Front End Concentrator Card, Digitizer Card and Scaleable Readout Unit

The ADC (**A**nalogue **D**igital **C**onverter) board in combination with the FEC (**F**ront **E**nd **C**oncentrator) board is placed after the APV board in the readout-chain. The ADC can be connected to up to eight APV pairs via HDMI cables and supports up to 2048 input channels. The ADC/FEC board receives the trigger signal, for example from a scintillator which it uses for the readout of the APV boards.

The ADC has two octal 40MHz ADC chips to convert the analog signal from the APV boards into digital data at a rate of 40MHz. The data is then merged by the FEC, which transmits the data to the DAQ (**D**ata **A**cquisition) or a SRU (**S**calable **R**eadout **U**nit). The SRU can merge data from multiple FEC cards before sending it to the DAQ. The raw data collected by a PC contains all the charge values equipped with additional information, such as the event number, a time bin number, a strip number, an APV channel number and an APV ID number.

The FEC card can be configured in different modes. In standard configuration, it transmits all data received from the ADC. In zero suppression configuration, the FEC only outputs channels with an active signal as the data volume may exceed the available 1GB/s bandwidth of an Ethernet connection in case of a trigger rate of about 1.2 kHz, an event length of 18 time bins and 16 APV boards in use [10].

3.5 False Sampling

The charge values which are sent in pulses by the APV to the ADC should resemble a step function in theory but are rounded off in reality, as shown in Fig. 3.6. This is due to the finite bandwidth of cables and connectors, which particularly cut the high frequency parts of the step function.

The shape of the real signal is due to the limited bandwidth of the APV and RC effects of the HDMI cable. The sampling phase at which the signal is picked off for

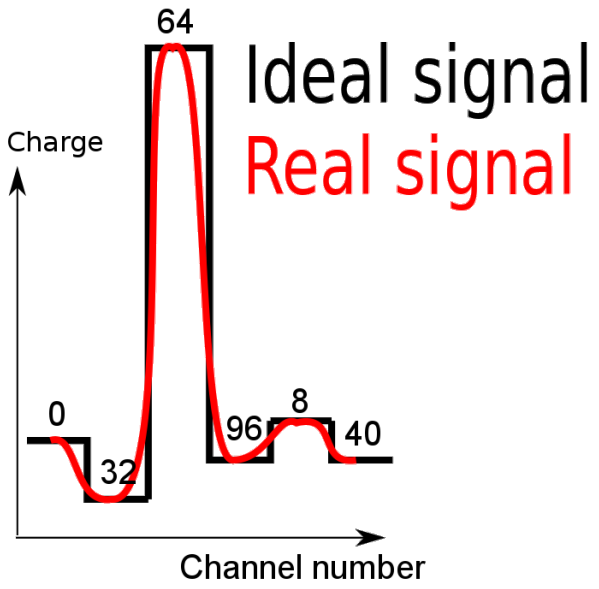

Figure 3.6: Analog signal from the APV board in the time frame of the ADC. Additionally the channel numbers of the charge values are noted in the diagram.

digitization can be tuned in the FEC configuration. A further source of distortion arises from the sampling process. As previously mentioned, slave APVs send their signal via the master APV and slave and master APVs are connected by an 16 pin cable. This results in a small phase shift of the signal from the slave APVs and ultimately the sampling phase is slightly shifted for the slave APVs. This affects the height of the charge values and can lead to fake signals for the proceeding channels in the sending order on the slave APVs.

Chapter 4

Data Acquisition

4.1 Data Acquisition at the Cosmic Ray Facility

For the study of signal distortion and development of correction methods a measurement with cosmic muons was performed using a large micromegas chamber in the CRF (**C**osmic **R**ay **F**acility) in Garching near Munich. The setup can be seen in Fig. 4.1. Here, one run with about 50000 events was recorded.

4.1.1 Experimental Setup

The L1 chamber has an active area of 102cm x 92cm and the detector is of the resistive strip type. It has an amplification gap of $128\mu m$ and a drift gap of 5mm. The drift voltage was set to 300V and the amplification voltage was set to 570V. The detector has 2048 readout-strips with a strip width of 0.3mm, a strip pitch of 0.45mm and a strip length of 102cm. It was operated with an $Ar:CO_2$ gas mixture with a ratio of 93:7. 8 APV pairs, one ADC card, one FEC card and one SRU were used for the readout.

A row of trigger scintillators is installed above the L1 chamber. The APV chips were configured with a PLL phase of 0, i.e. master and slave run synchronously, and the readout was configured to have 27 time bins per event.

A detailed detector analysis can be found in [6].

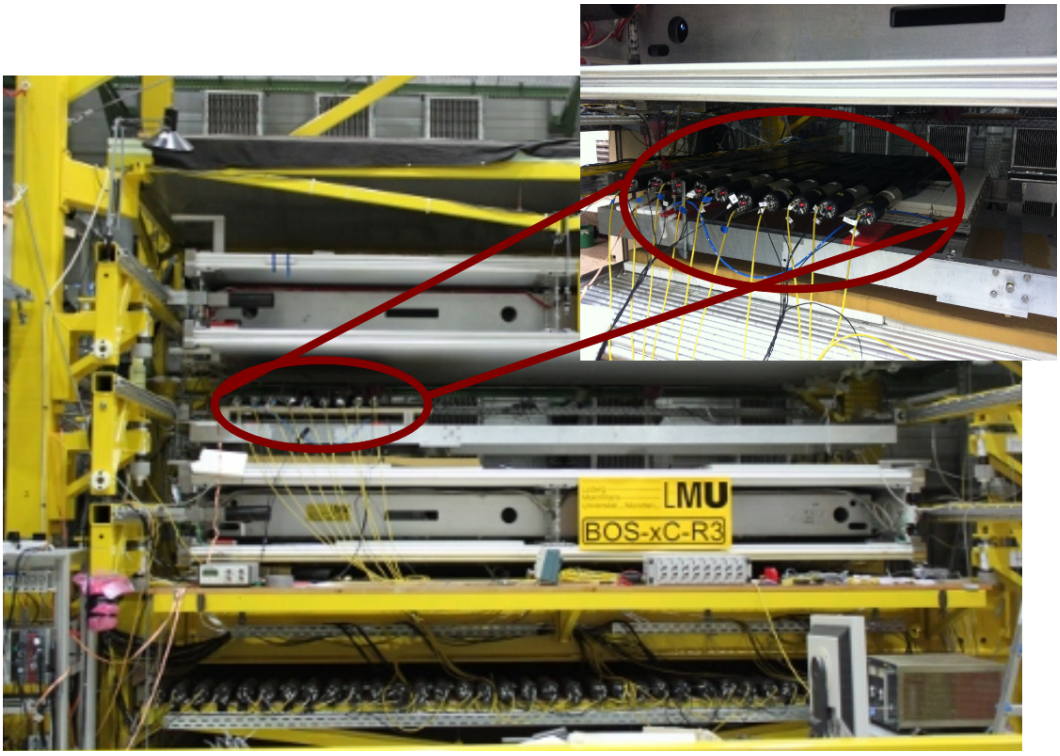

Figure 4.1: Picture of the L1 chamber at the CRF.

4.2 Data Acquisition at the Tandem Accelerator

To test the signal correction methods which are described in chapter 5, further data was acquired at the Tandem van de Graaph linear accelerator in Garching near Munich. The measurement was done with a micromegas telescope consisting of two two-dimensional and two one-dimensional floating strip micromegas detectors, which were placed into a 23MeV proton beam with a hit rate ranging from 100Hz up to 2kHz. A picture of the setup can be seen in Fig. 4.2. A total of 100 runs were recorded.

Protons exit the beam pipe and traverse the micromegas tracking telescope. Here the first detector doublet is inclined by -30° and the second detector doublet is inclined by +30°. A scintillator with photo multiplier is used as a trigger for signals.

4.2.1 Experimental Setup

The micromegas telescope consists of four micromegas, see Fig. 4.3, which had an active area of 6.4cm x 6.4 cm each.

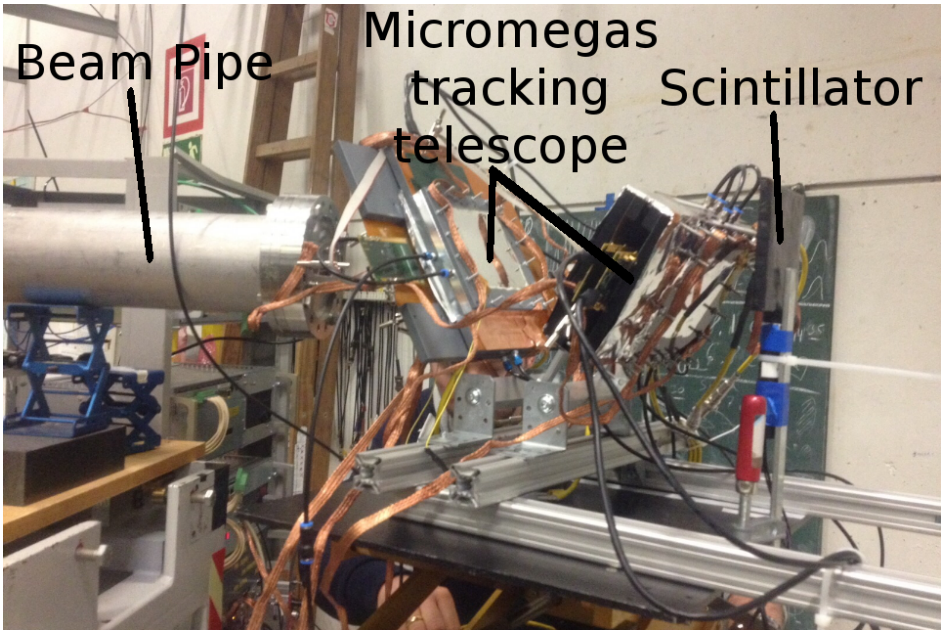

Figure 4.2: Experimental setup at the tandem accelerator.

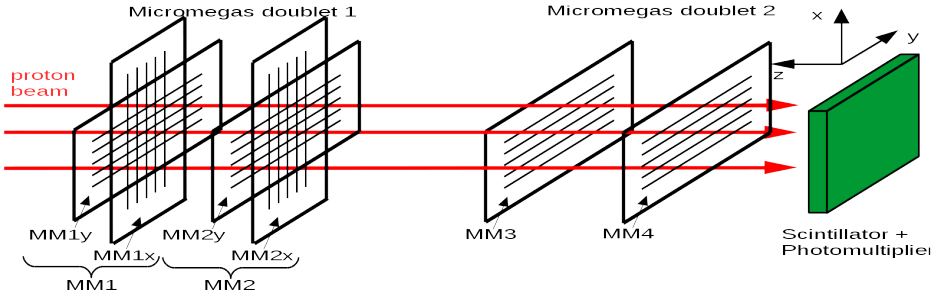

Figure 4.3: Scheme of the micromegas telescope. The x-layer of the first detector MM1

The detector planes had 128 strips with a strip pitch of 0.5 mm, a strip width of 0.3 mm and a strip length of 64mm. The detectors had an amplification gap of 150μm and a drift gap of 6mm. The detectors were operated with an gas mixture of $Ne{:}CF_4$ with an ratio of 80:20. The first detector doublet was build out of two two-dimensional micromegas MM1 and MM2 which were mounted back to back. MM1x/MM2x is the readout-layer directly underneath the floating strips and followed by the second readout-layer MM1y/MM2y. The second detector doublet consisted of two one-dimensional micromegas detectors MM3 and MM4 which were also mounted back to back. The orientation of the layers can be taken from Fig. 4.3. The amplification region of the first detector doublet contained bigger pillars in the amplification region and had printed resistors whereas the resistors of the second doublet were soldered. The doublets could be rotated around the y-axis. The standard voltage configuration for the drift and amplification region and the resulting field strengths of the detectors in the telescope are given in the following table:

Detector:	MM1	MM2	MM3	MM4
V_{drift}	200	200	200	200
kV_{drift}/cm	0.3	0.3	0.3	0.3
V_{ampl}	545	530	510	520
kV_{ampl}/cm	36.3	35.3	34	34.7

Table 4.1: Standard voltage/field strength configuration for the micromegas detectors of the telescope.

The chosen configuration showed well formed signals in a first short detector analysis on site.
The readout-chain is shown in Fig. 4.4. MM1 and MM2 were read out by a master-slave APV pair each. MM3 and MM4 were read out by a single master APV each. The signals were then further processed by an ADC+FEC unit. A scintillator was used as trigger and connected to the FEC board. The data was then stored on a PC.

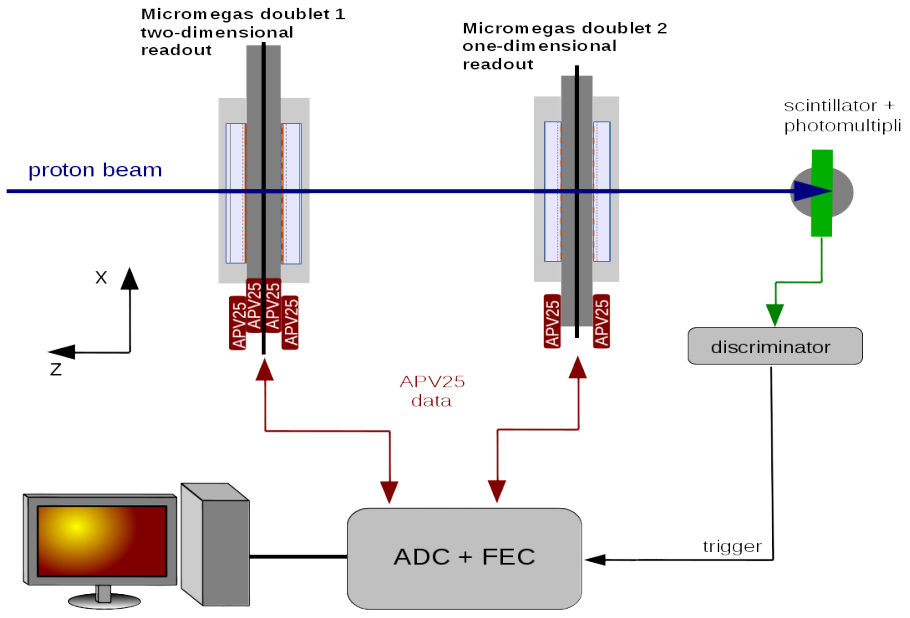

Figure 4.4: Scheme of the experimental setup at the tandem accelerator. The four micromegas detectors are read out using APV chips. Data was collected using an ADC+FEC unit. A scintillator was used for triggering signals. Data was then collected on a PC.

Data was recorded in five different FEC configuration modes: The standard FEC configuration with all strips read out, a dynamic range, a long timing and a short timing configuration. The configuration files differ in the values of the APV configuration. An overview is given in table 4.2.

Configuration:	config_FEC	config_FEC_dyn_Ber	config_FEC_short	config_FEC_long
APV_CSEL	247	254	247	247
APV_IMUXIM	16	10	16	12
APV_IPRE	100	100	98	240
APV_ISHA	34	34	34	5
APV_VFP	30	40	30	30
APV_VPSP	40	30	40	40

Table 4.2: Overview over the different configuration files showing the differences in the APV configuration settings.

Chapter 5

Signal Correction Methods

5.1 Signal Identification

As mentioned in chapter 3, the acquired data from the measurement was collected in raw data format on a PC. In the raw data, the charge values of the strips are available in a predefined time range, which is ideally chosen larger then the signal length. A visualization of the data for a section of the L1 chamber can be seen in Fig. 5.1.

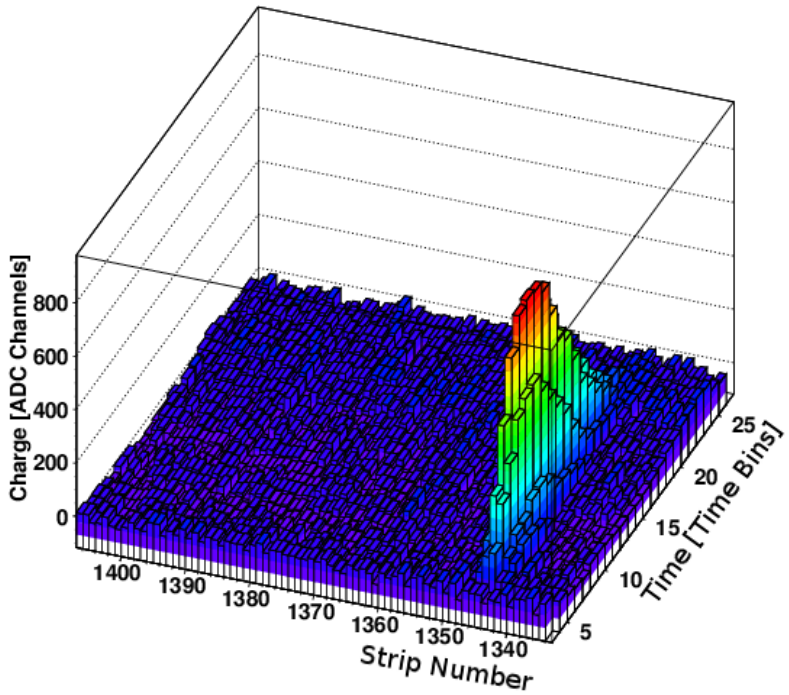

Figure 5.1: Charge values for a section of the L1 chamber plotted versus the time in time bins and the strip number.

Here, the charge values are plotted versus time and strip number. Most strips show only little variations around the zero value. On some strips, the charge rises very quickly

before declining again. The rise is due to a charging of the respective readout-strips due to an accumulatin of electrons created in an avalanche-like process in the amplification region and the decline is due to their relaxation. This behaviour correspods to a physical signal. A group of neighbouring strips displaying signals is called a cluster. From the cluster properties, the trajectory of the traversing particle can be partially reconstructed.

For signal identification the mean value and the variance of the strips in two different ways. In the following, the average charge value of a channel will be referred to as pedestal and the variance of a channel as its sigma.

The first method compares the sigma of a strip σ_{strip} for the event with the average sigma calculated for the same strip $\bar{\sigma}_{strip}$ over the first 500 events.

$$\sigma_{strip} \geq 3\,\bar{\sigma}_{strip} \tag{5.1}$$

If inequality 5.1 is fulfilled then the strip is said to have a signal.

Another and more sophisticated way is to calculate the pedestal and sigma event-by-event for each channel on one APV and then average over all sigmas of the APV.

$$\sigma_{strip} \geq 2.5\,\bar{\sigma}_{APV} \tag{5.2}$$

The strip shows a signal if the sigma of the strip exceeds 2.5 times the sigma of the APV, where 2.5 is an empirical value. This method showed better signal identification in cases with a lot of common mode noise on the channels.

5.2 Common Mode Noise Correction

For the common mode noise correction, it is assumed that all channels show the same noise behaviour. Signals are identified using condition 5.2. First off each channel its minimum charge value is subtracted. Then the charge values of all channels without signal are averaged for each time bin seperately, giving the common mode noise correction signal. Finally the correction signal is subtracted off all channels on the APV. Better signal identification was seen when the common mode noise correction was applied twice in a row.

5.3 Baseline Shift Correction

The baseline shift is caused by the design of the APV chip, as all pipelines of the chip are powered by the same source, as explained in chapter 3.3. The properties of the baseline shift were studied in detail with data acquired at the Cosmic Ray Facility, in the previous chapter 4.1.

The baseline shift was studied dividing the APV chip into halves, Fig.5.2.

The charge values were corrected by subtracting the pedestals and signals were identified by comparing the sigma of the channel for the individual event to its average

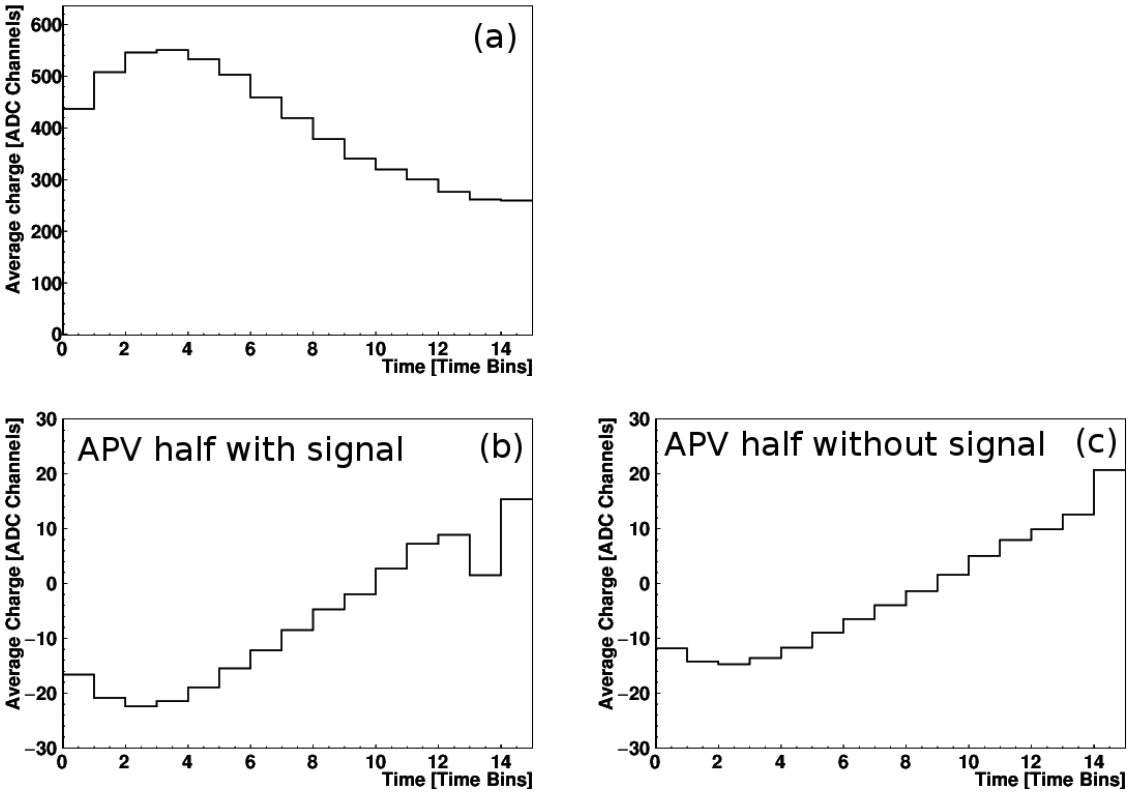

Figure 5.2: In (a) the cluster charge, in (b) the baseline shift on the APV half with the cluster and in (c) the baseline shift on the APV half without the cluster is plotted versus time.

sigma, like in Eq. 5.1. Here, the pedestals and sigmas calculated by the FEC configuration were used. The signals were then sorted into clusters, where a cluster had to consist of a minimum of two strips, and gaps of one strip in between the signals were allowed. For all clusters laying completely on one APV half without another cluster laying on the same APV the charge of the cluster was calculated for each time bin and the time bin where the cluster charge first exceeded 600 ADC channels was stored as a threshold value. Then, three diagrams were filled where the time coordinate fulfilled the following relation.

$$bin_t = t - t_{600ADC} \tag{5.3}$$

Relation of the bin_t to fill to the time bin of the charge value t and the threshold value t_{600ADC}. The diagrams were filled with the cluster charge, the baseline shift of the APV half the cluster lay on and the baseline shift of the other APV half. The baseline shift was calculated for each time bin averaging over the charge values of all channels without signal on the corresponding APV half. The diagrams in the Fig. 5.2 show the average charge values for the whole run with approximately 50000 events.

A baseline shift can be seen on both APV halves. On the APV half with the cluster, the baseline shift is stronger. On both APV halves, the baseline shift shows the same behaviour in time. Compared to the cluster charge the baseline shift reaches its minimum at the same time the cluster charge reaches its maximum. The baseline shift

then returns to zero faster then the cluster charge and exceeds zero in the end. This shows that the baseline shift cannot be reduced to one APV half. In fact the diagrams show the distance dependency of the baseline shift. The exceeding of the zero value for the baseline shift at the end can be explained by Lenz's law which can be seen as an equivalent of the energy conservation law and Newton's third law for electrical currents.

Next, the distance dependency of the baseline shift was investigated in more detail, as shown in Fig. 5.3.

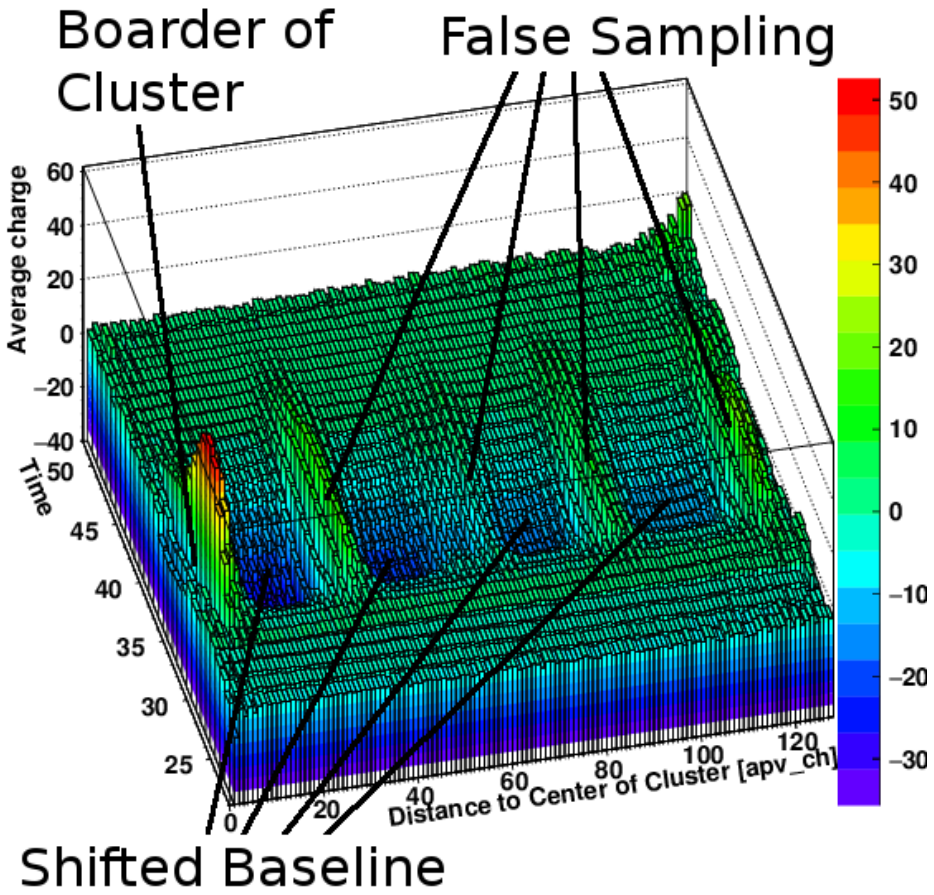

Figure 5.3: Average charge on channels without signal plotted versus the distance to the center of gravity of the cluster in channel numbers and time.

The same charge value correction, signal identification and cluster construction methods were used as before. It was checked whether the cluster laid on only one APV and that there was no other cluster on the APV. For each cluster and for each time bin the cluster charge and the center of gravity of the cluster in channel numbers was calculated. The time when the cluster charge first exceeded 600 ADC channels was stored as a threshold value. The relation between the coordinate of the time axis bin_t of the diagram, the timing of the charge value t and the threshold value t_{600ADC} is given in Eq. 5.4.

$$bin_t = t - t_{600ADC} + 28 \tag{5.4}$$

The cluster charge values were then filled into a diagram using Eq. 5.4 for the time

coordinate. The result can be seen in Fig. 5.4. Then the average charge values of all channels on the same APV without signal were plotted versus time and distance to the center of the cluster in channel numbers. The relation of the distance coordinate bin_{dist} to the channel number n of the strip and the center of gravity of the cluster at the time t cog(t) is given in Eq. 5.5.

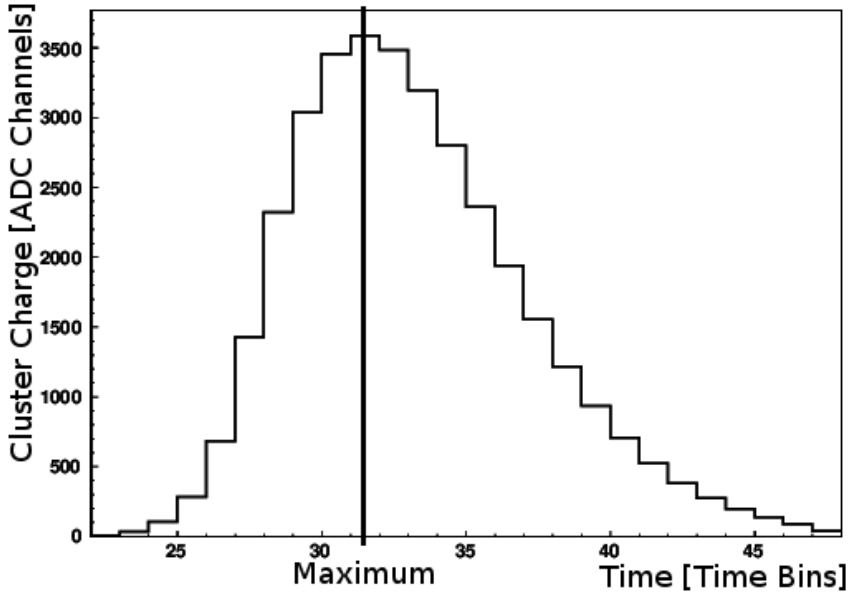

Figure 5.4: Average cluster charge plotted versus time.

$$bin_{dist} = |n - cog(t)| \tag{5.5}$$

The result can be seen in Fig. 5.3.

Most of the channels show the expected baseline shift which also shows the expected distance dependency as it is forms "valleys" which get deeper the nearer they are to the center of the cluster. But there are some regions which show a signal-like shape. One region is very close to the center of the cluster, while the other regions have distances of about 32, 64 and 88 channels to the center of the cluster. The signal like shape on the channels close to the center of the cluster can be explained as the contribution of signals which were too small for detection. The signal-like shape of the other regions can be explained as the contribution of signals from false sampling which were also too small for detection, since those are exactly the distances for two consecutive channels in sending order, as demonstrated in chapter 3.1.

The top view of Fig. 5.3 can be seen in Fig. 5.5. It shows that only channels with even distance to the center of the cluster show a signal-like shape. This can be explained by the distances in sending order for consecutive channels. Neighbouring strips in the detector usually have a distance of two in channel numbers, see Fig. 3.4, meaning that the signals at the boarder of the cluster are also evenly distanced.

The diagram was then redrawn omitting all channels with an even distance from the center of the cluster, as shown in Fig. 5.6. The baseline shift and its distance dependency can now be seen very nicely, as no channels with a signal-like shape show up in

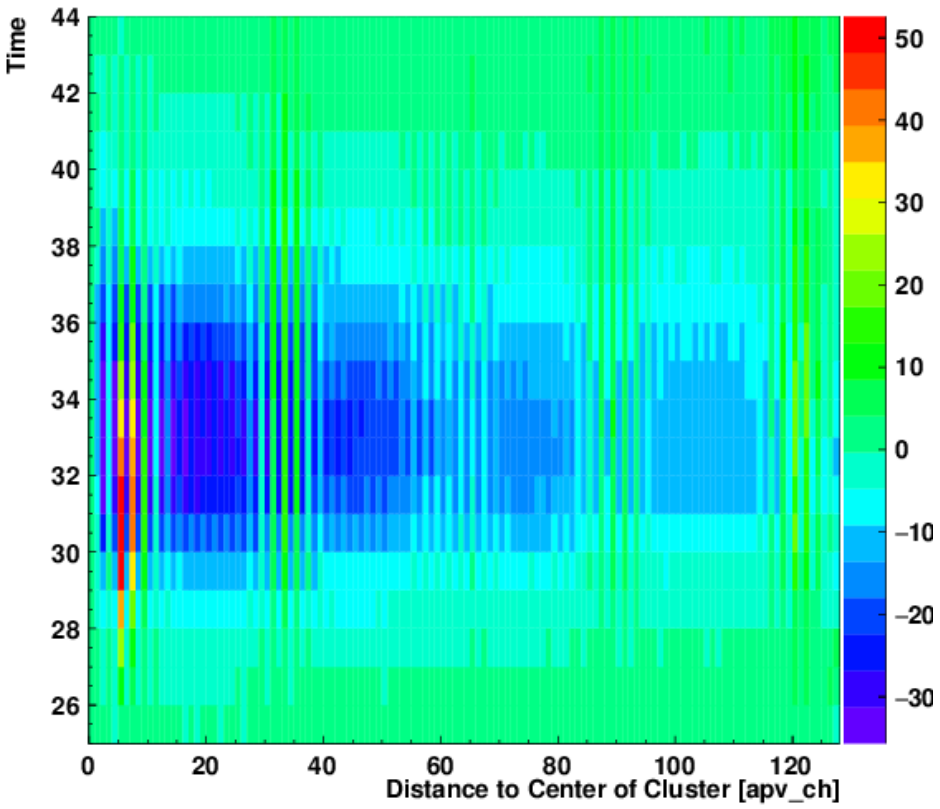

Figure 5.5: Top view of Fig. 5.3.

the diagram. Comparing the baseline shift to the average cluster charge in Fig. 3.5, the baseline shift reaches its minimum one time bin before the cluster charge reaches its maximum. Again, the baseline declines as the cluster-charge rises, until the maximum of the cluster charge is reached. Subsequently, the baseline shift levels out more quickly than the cluster charge.

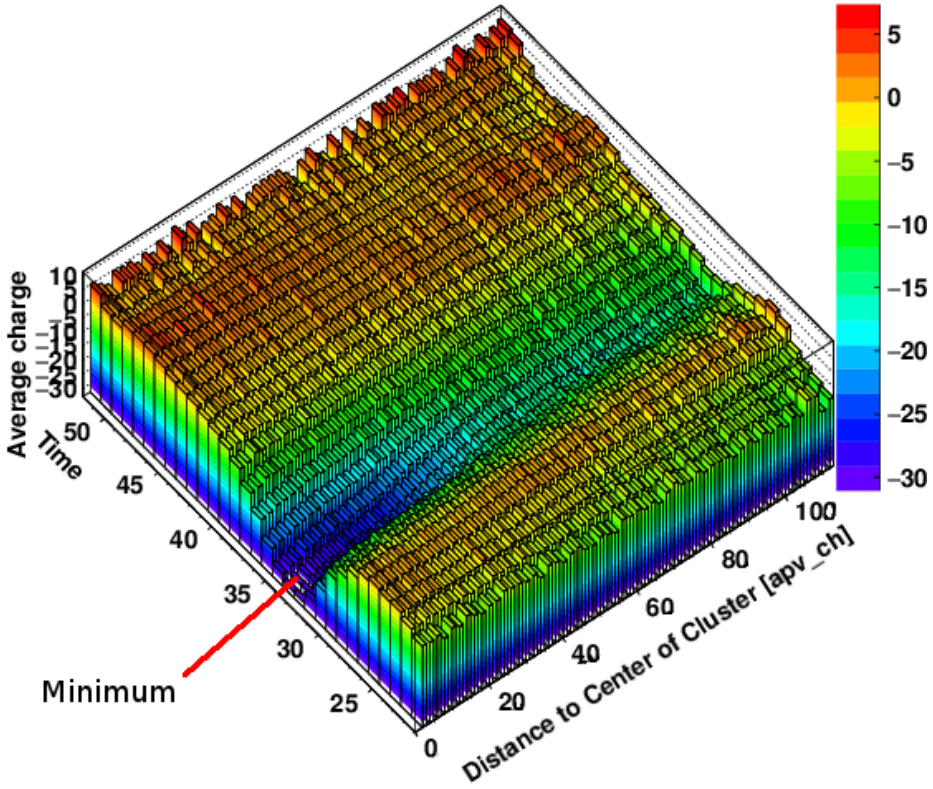

Figure 5.6: This is the same diagram, as in Fig. 5.3, but here only channels with an odd distance to the center of the cluster have been considered.

A cross section of the diagram in Fig. 5.6 at t=32 is shown in Fig. 5.7. The baseline shift has a linear distance dependency for channels with a distance of less than 64 channels from the center of gravity of the cluster.

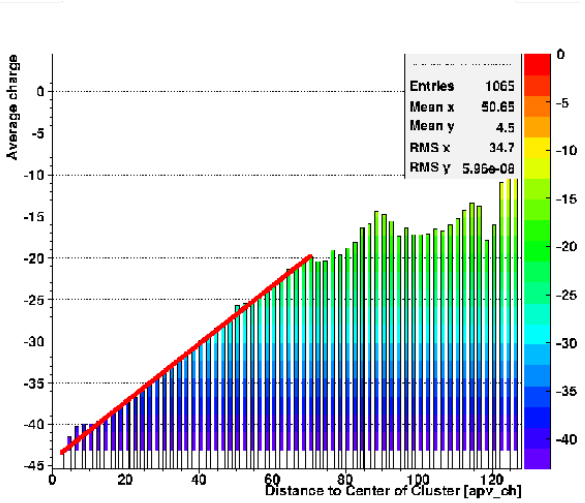

Figure 5.7: Crossection of Fig. 5.6 at t=32 fitted with a straight line.

Therefore, the baseline shift at the center of the cluster can be calculated by averaging the charge values of channels with an odd distance of less then 64 channels to the center of the cluster. For each channel, a weight has to be considered since the baseline shift is distance dependent. The weight w_i for the ith channel is expressed in terms of the center of gravity of the cluster $cog(t)$ at the time t and its channel number n by the following equation:

$$w_i = \frac{128}{128 - |cog(t) - n|} \tag{5.6}$$

Finally, the baseline-shift signal is multiplied by the average of all weights w_i. The baseline shift was caluculated averaging over all channels with an odd distance of less than 64 channels to the center of the cluster with weighting (Fig. 5.8 (a)) and without weighting (Fig. 5.8 (b)). The minimum of the weighted baseline shift is 34% lower than the minimum of the unweighted baseline shift.

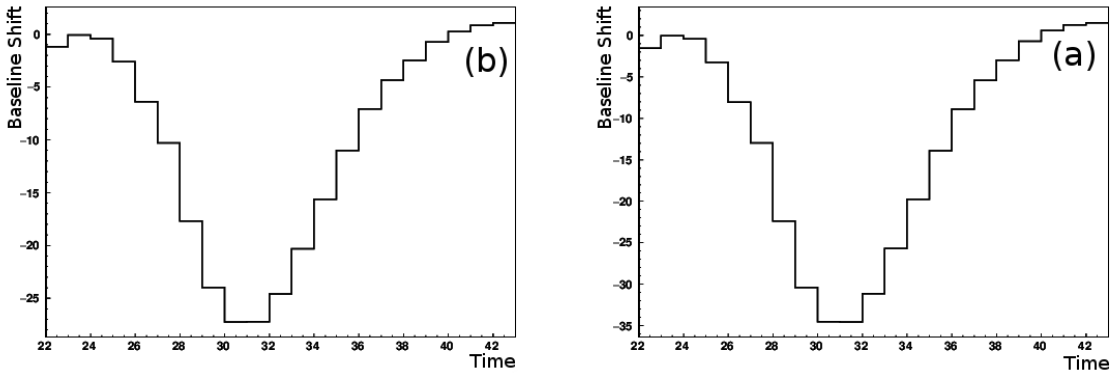

Figure 5.8: The baseline shift was calculated for channels with an odd distance of less than 64 channels to the center of gravity of the cluster without weighting on the left and with weighting on the right.

To determine the baseline shift as a function of the cluster charge, the weighted baseline

shift was plotted versus the cluster charge for each time bin, as shown in Fig. 5.9. Relation 5.4 was used to determine the time coordinate. A linear function was fitted to the resulting distribution:

$$f(x) = a * x \tag{5.7}$$

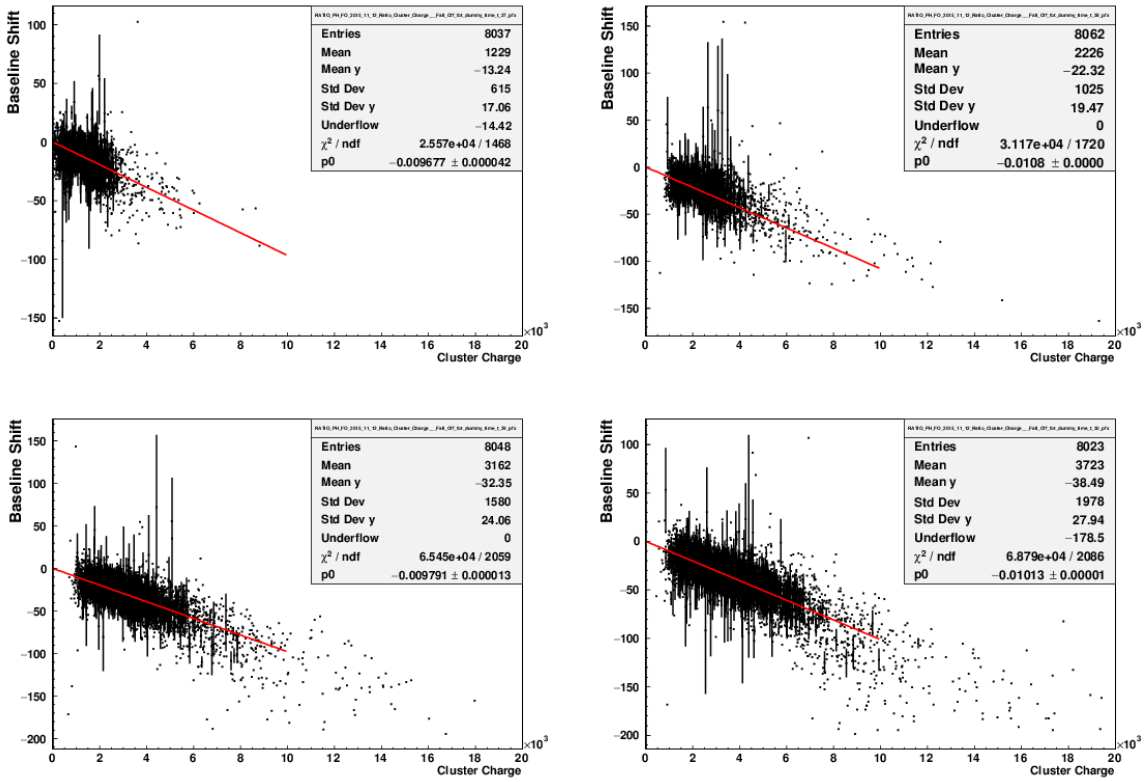

Figure 5.9: Examples of the diagrams with the weighted baseline shift plotted versus the cluster charge for each time bin. The upper left diagram shows the relation for t=$t_{600ADC} - 1$, the upper right for t=t_{600ADC}, the lower left for t=$t_{600ADC} + 1$ and the lower right for t=$t_{600ADC} + 2$.

The parameter a was calculated from the fit of function 5.7 to the baseline-shift versus cluster-charge diagrams in Fig. 5.9 and are shown in the table 5.1. The error of the fit parameters is negligibly small, as seen inf Fig. 5.9.

t	0	1	2	3	4	5	6	7
a	0	-0.0062	-0.0088	-0.0097	-0.0110	-0.0098	-0.0100	-0.0097
t	8	9	10	11	12	13	14	15
a	-0.0094	-0.0077	-0.0075	-0.0064	-0.0048	-0.0040	-0.0022	0

Table 5.1: Correction coefficients a for the baseline shift.

In Fig. 5.10 the fit parameter a is plotted versus time.

The baseline shift can now be corrected by multiplying the cluster-charge values with the correction coefficients in table 5.1 after matching those values via the threshold value. The threshold value corresponds to the fourth coefficient in table 5.1.

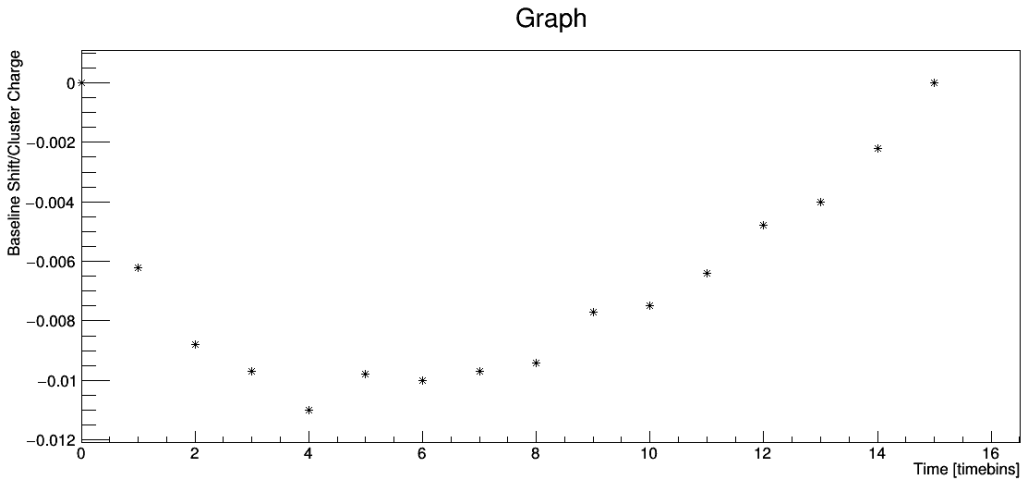

Figure 5.10: Correlation coefficients of baseline shift and the cluster charge.

The threshold value could be improved by determining the inflection point of Fermi function fitted to the cluster charge.This would lead to a more precise comparability of the cluster charge with the baseline shift.

5.4 Phase Shift Correction

As mentioned in chapter 3.5, false sampling can lead to fake signals in the readout-data. This effect was studied using the data acquired at the cosmic ray facility (see chapter 4.1). Signals were identified using relation 5.1. Then, the maxima of the signals and their corresponding time t_{max} as well as the charge value of the following channel in sending order at $t = t_{max}$ were determined. Subsequently, the values were plotted in two diagrams, one for the master APVs and one for the slave APVS. The result can be seen in Fig. 5.11.

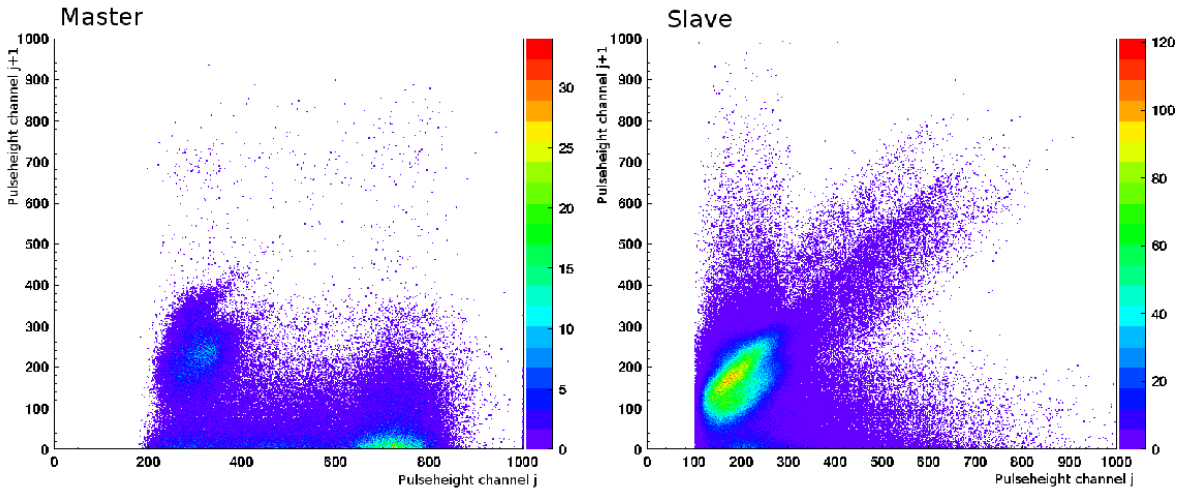

Figure 5.11: Charge values of two consecutive channels in sending order plotted against each other for master APVs and for slave APVs. j is the sending number of the strip.

For the master APVs, there is almost no correlation between the signals of two con-

secutive channels. Many channels show a pulse height between 600 and 800 ADC channels but lower signals were also taken into the diagram. The charge values of the consecutive channels seem to be randomly distributed. Only in the region around 300 ADC channels a correlation of the signal on consecutive channels, can be found, but this can be explained by common-mode noise which not only leads to false signals but commonly affects multiple strips with equal strength.

The distribution is different for the slave APVs. Their signals show lower maxima and the charge values on consecutive channels show strong correlation, jut as predicted by the theory (see chapter 3.5).

The fact that fake signals occur for consecutive channels in sending order and that real physical signals form clusters can be used for fake signal identification. Fake signals can also form clusters, usually they are smaller, because the distance in strip numbers for consecutive channels in sending order takes on distinct values.

A phase shift correction was implemented for the cosmic ray facility data, which was used for identifying and then sorting all signals into clusters. By sorting the signals into clusters alone, a lot of signals are ignored. The remaining clusters can then be searched for signals on consecutive channels in sending order. As preveiously mentioned, the cluster with the fake signals should have a lower charge than the physical one. For this purpose, the fact that the detection rate of this detector was too low for multiple particle detection was used. Only the biggest clusters were kept. The following table presents the efficiency of fake signal(=F.S.) detection for the experimental data.

Total Signals	F.S. in Cluster	F.S. not in Cluster	F.S. Total
117441	2680	85345	88025

Here the number of signals, the number of fake signals in clusters, the number of fake signals outside clusters and the total number of fake signals is given. 97% of the fake signals are sorted out as they don't form clusters. Only 3% of the fake signals show up in clusters. For low hit rates it is therefore sufficient to only consider the biggest cluster to omit fake signals.

Chapter 6

Detector Analysis of the Tandem Setup

To verify the corrections developed previously in chapter 5, the angle between the beam axis and the second detector doublet of the Tandem setup will be reconstructed in the following chapter 7. Then, the second detector doublet was chosen, because of the following detector analysis. Here, the pulse height of the leading cluster, the number of strips hit, the hit efficiencies and the number of clusters were plotted versus the amplification and the drift field. In the following diagrams errors obtained from the fits were used, if they are not visible then they are smaller than the the marker size. The data was analyzed using an analysis code written together with B. Flierl.

6.1 Detector Analysis

In the following, the naming of the detector scheme in Fig. 4.3 was used. For the detector analysis the amplification and drift field were varied separately for each detector, while the other detectors were set to the standard configuration, which is described in table 4.1.

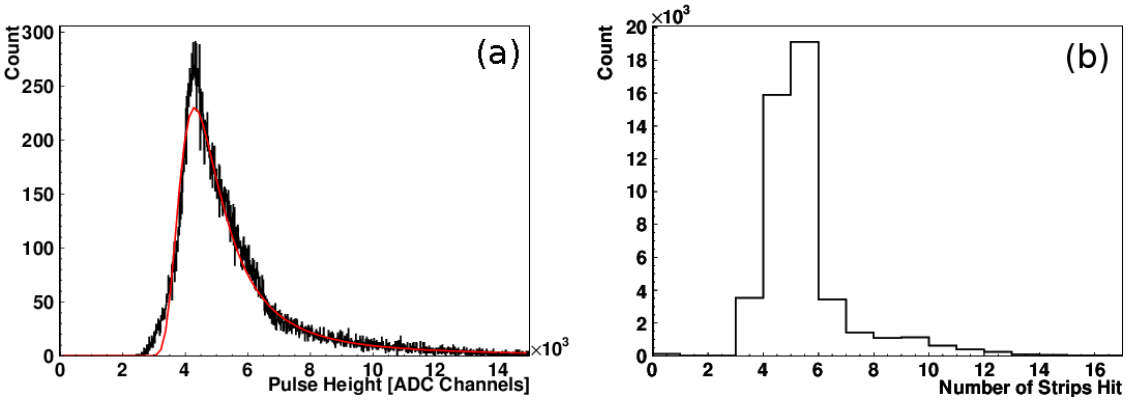

Figure 6.1: Leading cluster charge (a) fitted with a landau distribution and number of strips hit (b) for MM2x.

Fig. 6.1 shows the pulse height of the leading cluster charge and the number of strips

hit for MM2x for a drift field of 333V/cm and an amplification field of 35 kV/cm. The most probable value of the pulse height fit was then plotted versus the amplification field, in Fig. 6.2 (a), and the drift field, in Fig. 6.2 (b), for all detectors used in the telescope.

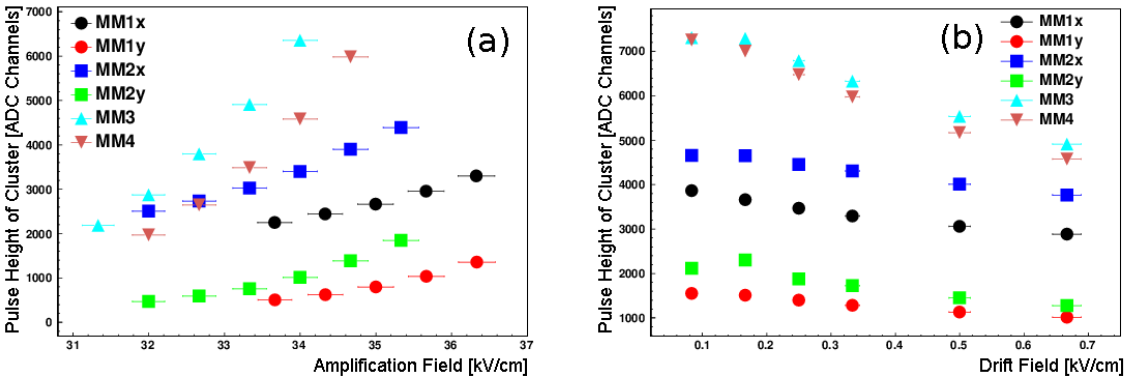

Figure 6.2: Leading cluster charge plotted versus the amplification field (a) and the drift field (b), for all detectors used in the telescope.

For all field strength configurations the y-layers of MM1 and MM2 showed a lower pulse height than the x-layers. Comparing MM1 to MM2: MM1x showed a lower pulse height than MM2x, the same is true for MM1y and MM2y. From the detector design it is clear, that the signals of MM1y and MM2y were smaller than the signals of MM1x and MM2x, since the x-layers are closer to the floating-strips and the y-layers are separated from the x-layers by a layer of insulating material. Although MM1 and MM2 are identical in design a higher pulse height was expected for MM2. For one thing, because the protons reached MM2 with a lower kinetic energy as they traversed the readout-planes of MM1 and MM2 first, before they entered the active gas volume of MM2. From the Bethe Bloch formula, Eq. 2.1, it follows that the ionization probability is higher for less energetic protons. Hence, more electrons were created in the drift region of MM2. This effect accounted for an increase in electron production of about 10%, as was argued in detail in the masters thesis of F. Klitzner [3]. For another thing, the protons were scattered at the readout-planes between MM1 and MM2. This led to a widening of the proton beam in MM2, which resulted in longer trajectories of the protons in the drift region of MM2, hence more electrons were created here. Additionally, the amplification region of MM1 could be bigger than designed, which would result in a lower pulse height for MM1, as discussed in detail in the dissertation of J. Bortfeldt [1].

MM3 and MM4 are also designed identically. For the amplification field scan MM3 showed a bigger pulse height than MM4. Since protons reached MM4 with less energy than MM3, the same arguments as previously mentioned should hold here and MM4 should have shown a higher pulse height than MM3. Nevertheless, a lower pulse height was observed for MM4, this could be due to a bigger than designed amplification gap of MM4.

The the first detector doublet showed a lower pulse height than the second detector doublet. For one thing, this due to the fact that only the y-layers of the first doublet are inclined to the beam axis. For another thing, this could be due to differences in the signal formation processes for one and two-dimensional floating-strip micromegas.

It is assumed, that the mirror charges of the ions in the amplification region on the floating and readout-strips give rise to the signals, but this has to be studied yet.

Fig. 6.2 (a) shows, that the pulse height of the cluster charge increased with the amplification field. This is because, the number of electrons created in the amplification region increases with the amplification field. Fig. 6.2 (b) shows, that the pulse height decreased with the drift field. This could be due to the fact, that the mesh transparency decreases with the drift field strength, which is discussed in detail in the dissertation of J. Bortfeldt [1].

In Fig. 6.3 the distributions of the pulse height of the cluster charge can be seen for all detectors in standard configuration.

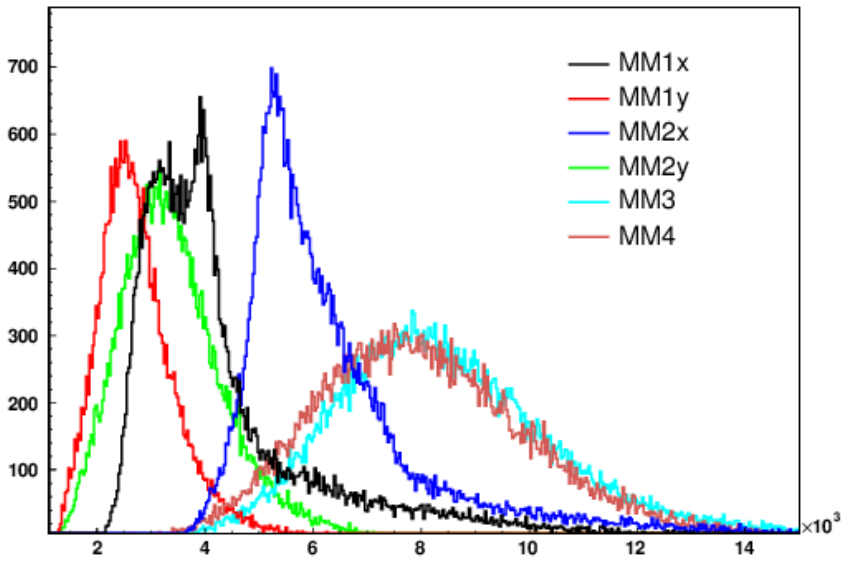

Figure 6.3: Pulse height distributions for all detector layers in standard configuration.

The distributions of the pulse height for MM1y and MM2y show the lowest mean values, which means that those layers detected small signals on very few strips. The mean value of the distribution for MM1x is much smaller than the mean value of MM2x, showing again, that MM1 was not operating well. The distributions for MM3 and MM4 are broader and show higher mean values than those of MM1 and MM2. This is due to the fact, that MM3 and MM4 are inclined to the beam axis whereas MM1x and MM2x are not.

The number of hit strips was plotted versus the field strength in Fig. 6.4.

For MM1 less strips were hit then for MM2. For one thing, this could be due to a deformation of the amplification region of MM1. For another thing, MM1 could have been grounded inferior to MM2. This would result in a higher sigma of the channels of MM1 and therefore a lower probability for the identification of signals. MM3 and MM4 show similar results in number of strips hit, although an increased number of hit strips for MM4 would be expected, since the proton beam is widened at the readout planes between MM3 and MM4.

The hit efficiencies were calculated for each detector layer of the telescope, using the

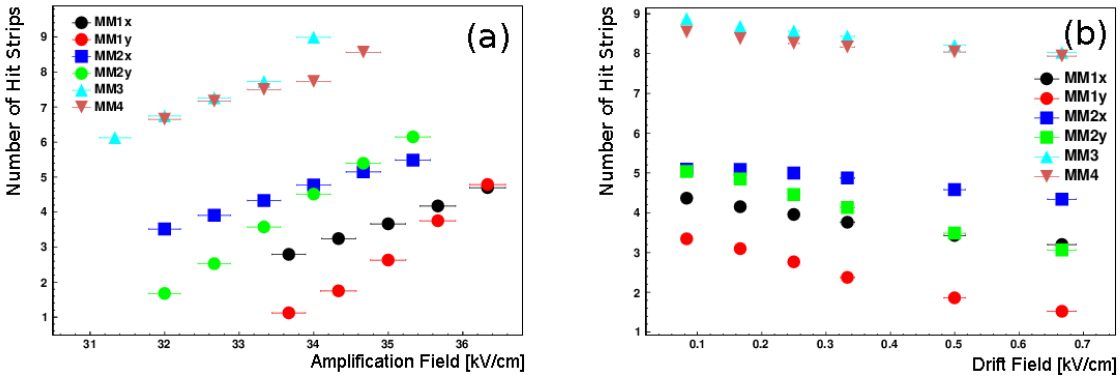

Figure 6.4: Number of strips hit plotted versus the amplification field strength (a) and drift field strength (b).

following equation:

$$e_l = \frac{N_{all}}{N_l} \tag{6.1}$$

Here the hit efficiency e_l is calculated as the fraction of the number of events with at least one cluster on all layers N_{all} divided by the number of events with at least one cluster on all other layers except the one under observation N_l. The hit efficiencies are plotted in Fig. 6.5.

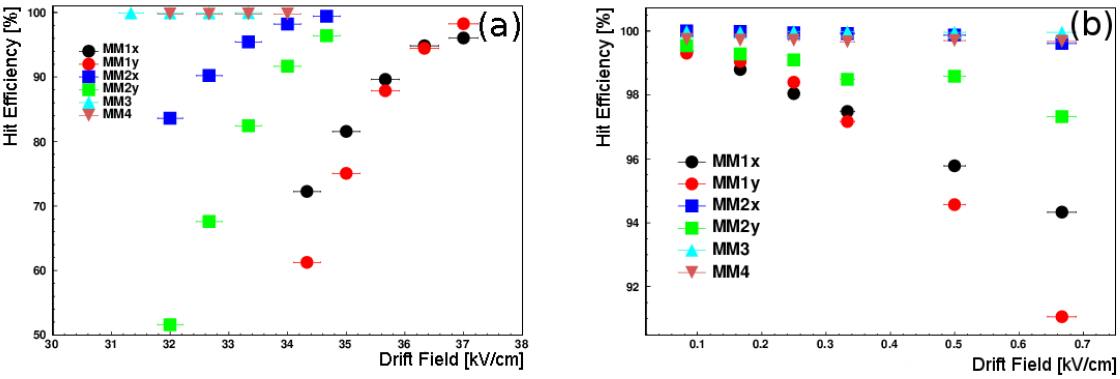

Figure 6.5: Hit efficiencies plotted versus the amplification field strength (a) and the drift field strength (b).

For MM1 and MM2 hit efficiencies increased with the amplification field and decreased with the drift field. Here the x-layers showed better hit efficiencies than the y-layers. The results should be considered with caution, since the hit efficiencies of the detectors are correlated. A detector with a low hit efficiency improves the hit efficiency of the other detectors. Moreover, the hit efficiencies obtained for the x- and y-layers of MM1 and MM2 shared the same field configuration.

MM3 and MM4 showed almost 100% hit efficiency for all configurations, this is due to the low hit efficiencies of MM1 and MM2.

For a better understanding of the hit efficiencies, the average cluster number was

plotted versus the field strength in Fig. 6.6.

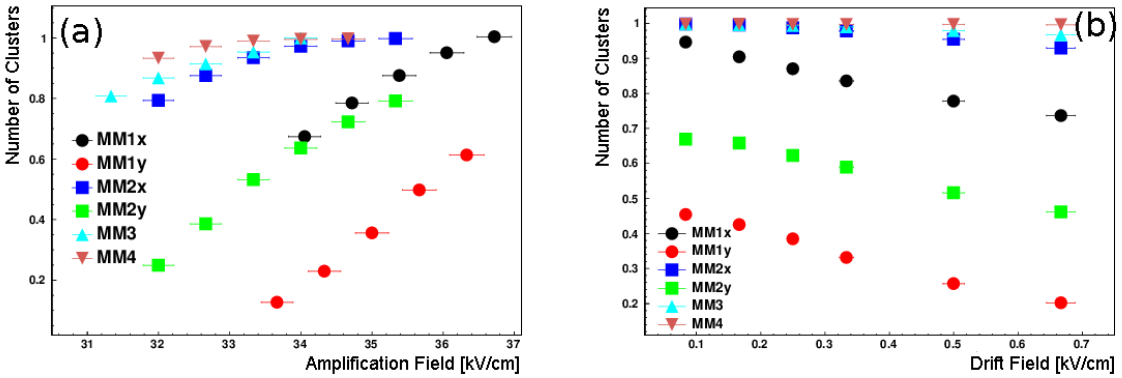

Figure 6.6: Cluster number plotted versus the amplification field (a) and the drift field (b).

For MM1 and MM2 the number of clusters increased with the amplification field, more than the hit efficiency increased with the amplification field. The cluster number for MM1 and MM2 decreased with the drift field, again stronger than the hit efficiencies. Therefore, the hit efficiencies of the x and y-layers of the first detector doublet can be assumed worse if only compared to the the second detector doublet. For MM3 and MM4 the cluster numbers increase the amplification field strength. Showing, that the hit efficiencies of MM3 and MM4 vary with the field strengths applied.

Therefore, for the verification of the corrections only the data from MM3 and MM4 will be used, because this detector doublet showed a good pulse height behaviour for the signal identification, a sufficient number of hit strips for the angle reconstruction and a high efficiency enabling a good comparability of results. As MM1y and MM2y lacked in terms of this qualities, their data was not further considered.

The drift and amplification field scans were realized for the different APV configurations of table 4.2. In the following the number of hit strips for the different configurations will be compared. The number of hit strips for MM3 was plotted versus the amplification field, in Fig. 6.7 (a), and the drift field, in Fig. 6.7 (b), for the different APV configuration files.

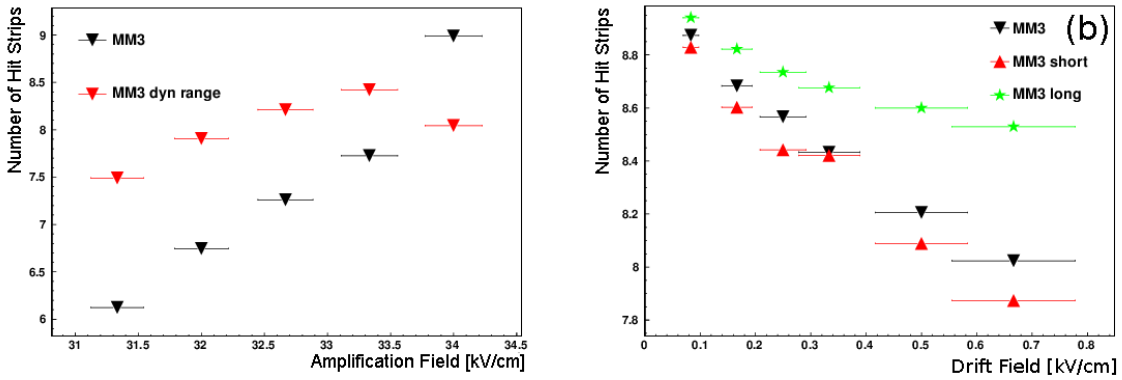

Figure 6.7: Number of hit strips for MM3 and different APV configurations

For MM3 the number of hit strips is higher for the configuration using a dynamic range

than for the standard configuration in the amplification scan . For the drift field scan the long configuration showed the highest number of hit strips.

Fig. **??** shows the number of hit strips plotted versus the amplification field and the drift field for MM4.

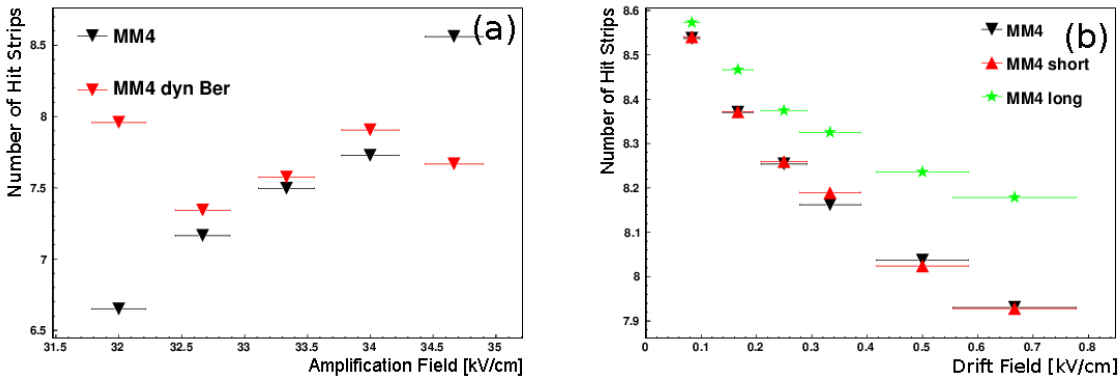

Figure 6.8: Number of hit strips for MM4 and different APV configurations

For MM4 the configuration use of the dynamic range or the standard configuration made no difference in the observed number of hit strips. For the drift field scan the long configuration showed again the highest number of hit strips.

Only the long configuration shows a higher number for both detector doublets. Therefore, the long configuration should enable a more precise reconstruction of the angle, as the μTPC-method, introduced in chapter 7.1, is dependent on the pulse height and the number of strips in the cluster.

6.2 Asymmetric Gaussian Fit

When investigating the center of gravity of hit positions for the leading cluster like in Fig. 6.9, an asymmetric distribution is found. The best way to determine the most probable value is to use an asymmetric gaussian function:

$$\begin{aligned} f(x) =& C_0 exp\left(-0.5\frac{(x-x_0)^2}{\sigma_r^2}\right) \quad \text{for} \quad x > x_0 \\ f(x) =& C_0 exp\left(-0.5\frac{(x-x_0)^2}{\sigma_l^2}\right) \quad \text{for} \quad x < x_0 \end{aligned} \tag{6.2}$$

The asymmetric gaussian function is expressed in terms of the overall scale C_0, the most probable x_0, the sigma, to the right side of the most probable value, σ_r and the sigma, to the left side of the most probable value, σ_l.

6.3 Angle Reconstruction for the Second Micromegas Doublet

The angle between beam axis and the second detector doublet can best be determined statistically. As seen in the scheme of the setup, in Fig. 4.4, the last two detectors were mounted back-to-back each other. The distance between the two readout-planes is $(31.5 \pm 1)\,mm$. Fig. 6.9 shows the distribution of the hit positions of the leading cluster for MM3 and MM4.

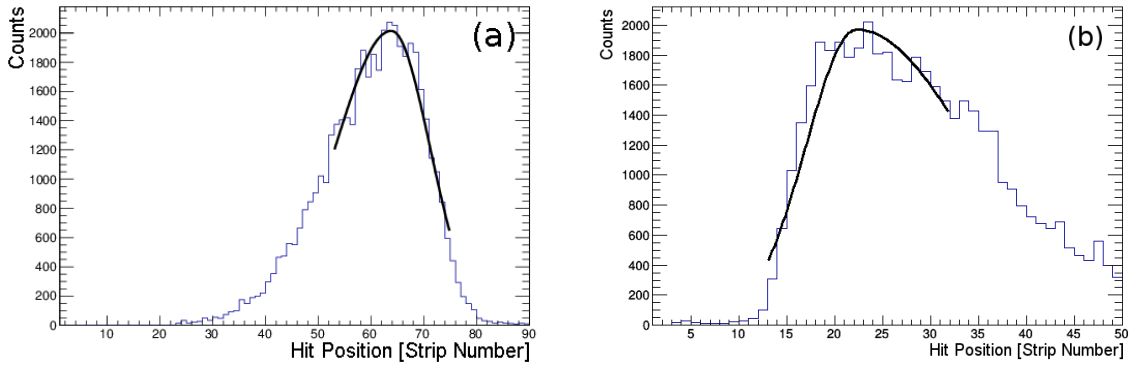

Figure 6.9: Distribution of the hit positions of the leading cluster plotted versus the strip number for MM3 (a) and MM4 (b).

The distributions were then fitted with an asymmetric gaussian function. The most probable hit position in strip numbers of MM3 was 63.9±0.5 and the most probable hit position for MM4 was 22.3±0.3.

The angle between the beam axis and the detector plane can then be calculated, considering the distance between the readout-planes of the two detectors and the difference between the average hit positions inside the detector, via the following formula 6.3.

$$\begin{aligned} \alpha &= \arctan\left(\frac{(a_1 - a_2)0.5\text{mm}}{31.5\text{mm}}\right) \\ \alpha &= 32.93^\circ \pm 0.01^\circ \end{aligned} \tag{6.3}$$

Calculation of the angle α between the second detector doublet and the beam axis, where 31.5mm is the distance between the two readout-planes, 0.5mm is the strip pitch and a_1=128-22.3+1 and a_2=63.9 are the most probable strip positions of the leading cluster on MM3 and MM4 respectively. For the calculation of a_1 it had to be considered that the readout plane of MM4 was inverted to the readout plane of MM3.

Chapter 7

Verification of the Corrections

The corrections were then integrated into an analysis program for micromegas telescopes written together with B. Flierl. To verify if the corrections improve the angular resolution of the data, acquired at the Tandem accelerator, the angle between the beam axis and the second detector doublet was reconstructed with the μTPC method. The reconstructed angles fro the corrected data were then plotted versus the amplification field and the drift field.

7.1 Single plane angle reconstruction - μTPC Method

With the data of a single readout-plane it is possible to reconstruct the angle α between the projection of the particle trajectory on a plane vertical to the readout-strips of the detector and the readout-plane.

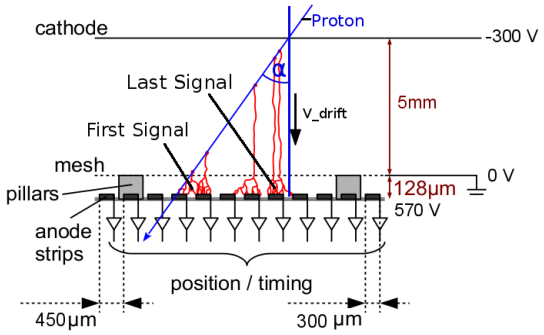

Figure 7.1: The different drift times of the electrons in the active gas volume lead to different timings of the signals. This can be used for the reconstruction the angle α.

The method is motivated by the difference in drift time of the electrons created in the ionization process by the traversing particle. Electrons, created closer to the micromesh, will sooner induce a signal on the readout-strips than the electrons which were created closer to the cathode.

From the cluster properties the angle can be reconstructed using Eq. 7.1.

$$\alpha = \arctan\left(\frac{p}{av_{drift}b}\right) \tag{7.1}$$

Here, the angle α is calculated with the cluster slope a, the strip pitch p, the drift velocity v_{drift} and the duration of one time bin b. The cluster slope a is obtained by a fitting a straight line to the signal timings of the cluster.

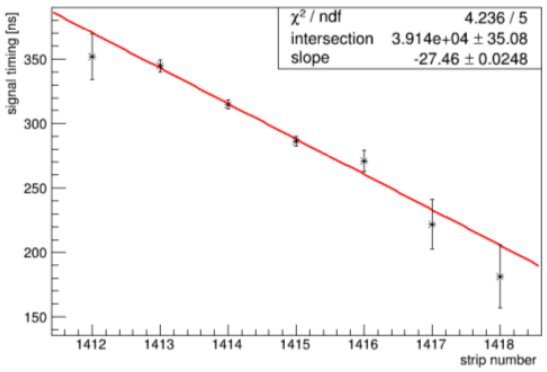

Figure 7.2: Timing of the signals of a cluster plotted versus the strip number. Taken from [6]

The timing was obtained as the inflection point of a Fermi function fitted to the signal.

7.2 Variable Binning

The reconstructed angles were then filled into diagrams. At this stage it was important to modify the width of the binning of the diagrams according to the arctan function:

$$\tilde{w}_{bin} = arctan\left(\frac{1}{\frac{n_{bin}}{N} w_{bin}}\right) \tag{7.2}$$

The width of a bin for diagram of the angular distribution $\tilde{w}_{bin}$, expressed in terms of the width of the w_{bin} for the diagram of the cluster slope distribution, the bin number n_{bin} and the total amount of bins in the cluster slope distribution N. This way it was ensured, that the distributions were not biased by the non linear transformation between cluster slope a and angle α. The bias can be seen in Fig. 7.3, which shows the angular distributions for MM4 in standard configuration for a binning with equal width (a) and for a binning with variable width (b). Note, that the distributions show different shapes and mean values.

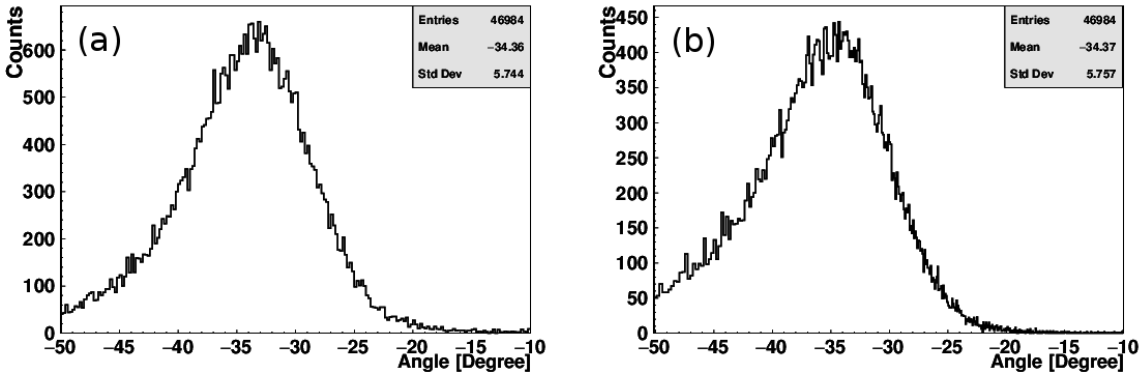

Figure 7.3: Angular distribution for MM4 with binning of equal width (a) and binning of variable width (b).

7.3 Corrections

Three different corrections were used to correct the data:

1. Baseline Shift, Common Mode Noise and False Sampling Correction
2. Common Mode Noise Correction by B. Flierl
3. Baseline Shift and False Sampling Correction

All corrections are done APV-by-APV and event-by-event, they are described in the following: (1.) This correction first corrects the common mode noise. For each channel the minimum charge value, the pedestal and the sigma σ_{strip} is determined. In the next step the average of the sigmas on the APV σ_{APV} is calculated, signals are now identified by comparing the sigma of a strip to the sigma of the APV. A channel has a signal if

$$\sigma_{strip} > 2.5 \cdot \sigma_{APV} \tag{7.3}$$

is fulfilled. The previously determined minimum is then subtracted off each channel. The common mode noise correction signal is calculated by averaging over the charge values of all non hit channels for each time bin separately. The correction signal is then subtracted off all channels on the APV. The common mode noise correction is applied to the data twice in a row, because it showed better signal identification. This is due to the fact, that for the second time the sigma of the strips is reduced enabling better identification of small signals. Then the baseline shift correction signal is calculated. Therefor, all signals are sorted into clusters, where gaps of two channels are admitted. The cluster charge is calculated for each time bin and the cluster with the biggest charge is identified. For the biggest cluster the value, where the cluster charge exceeded 600 ADC channels, is determined and stored as a threshold value. The baseline shift correction signal is calculated by multiplying the charge of the biggest cluster with the coefficients of table 5.3. The coefficients are matched using the threshold value. The baseline shift correction signal is then subtracted off all channels in the biggest cluster.

Only the channels of the biggest cluster were marked as signals suppressing fake signals from false sampling.
(2.) The common mode noise correction written by B. Flierl corrects the data in an analog way as the common mode noise correction of (1.). The only difference is, that the APV is here divided into two halves. The common mode noise is then corrected on both halves separately.
(3.) With this correction the baseline shift and the false sampling is corrected in the same way as in correction (1.). The difference is, that this correction could also be applied to zero suppressed data.

7.4 Comparison Corrected and Uncorrected Data

All three corrections were applied to the data of MM3 and MM4. The obtained angular distributions, with variable binning, were then fitted with an asymmetric gaussian function. In the following diagrams the error of the angle was taken from the fit, if the error bars are not visible then they are smaller than the marker size. Around the expected angle a range of $\pm 0.6°$ is shaded with red dots. In a second diagram the sigma values of the right σ_r and of the left side σ_l of the most probable value obtained by the fit were drawn, the sign σ_l was flipped enabling better comparability of the diagrams.

For MM3 the reconstructed angle was plotted versus the amplification field in Fig. 7.4. The angle was calculated using Eq. 7.1, with $p = 0.5mm$, $b = 25ns$ and $v_{drift} = 0.078mm/ns$, taken from the MAGBOLTZ simulation for $NeCF_4$ with an ratio of 80:20, as shown in chapter 2.3.
The reconstructed angle for the common mode noise and baseline shift correction (1.) was about 1° bigger then expected, but about 0.5° smaller then the angle reconstructed from the uncorrected data. Note, that the reconstructed angle for correction (1.) is the most stable. Correction (1.) shows the second smallest sigma values, comparing the right an the left sigmas individually to the other results. For this correction about 2/3 of the total events were considered in the calculation of the angle. The correction (2.) written by B. Flierl shows an angle about 1° smaller than expected and most distant from the angle reconstructed without correction. Nevertheless, this correction has the smallest sigma values and about 7/8 of total events were considered. The reconstructed angle from correction (3.) lies between the angles of the uncorrected and the noise and the data from correction (1.). Also the sigma values of correction (3.) lie in between the sigma values of the uncorrected and the data from correction (1.). The reconstructed angle is less stable than the angle obtained by correction (1.) but more stable than the angle of the uncorrected data. Here, almost all events were considered. The uncorrected data shows biggest deviation from the expected angle. The left and right sigmas in absolute values are bigger then those of all corrected.

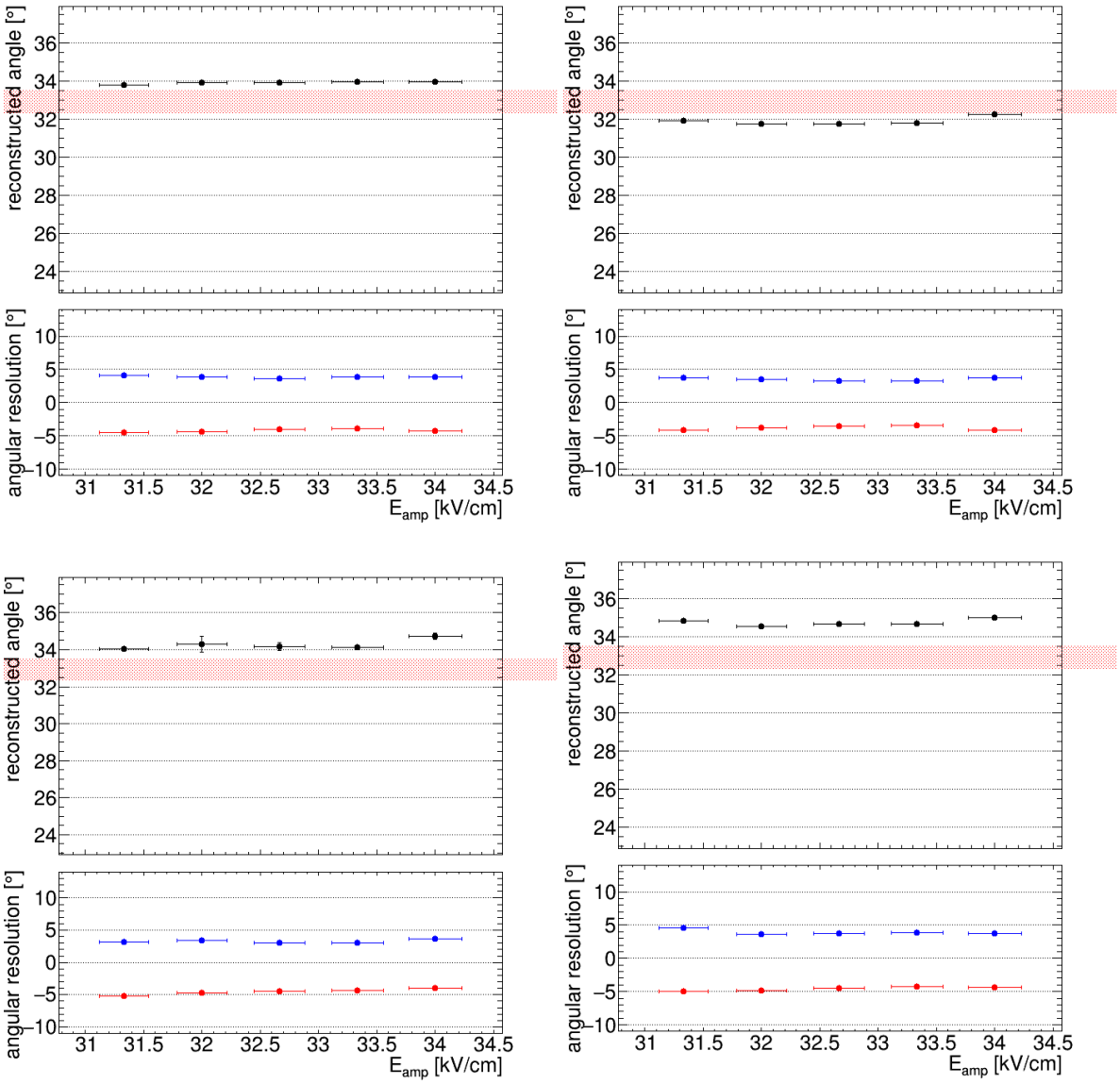

Figure 7.4: Angle of the beam axis and MM3 plotted for the different correction methods for standard FEC configuration. Common mode noise and baseline shift correction (top left), common mode noise correction by Bernhard Flierl (top right), baseline shift correction (bottom left), no correction (bottom right).

The reconstructed angles for MM4 can be seen in Fig. 7.7. The same observations as for MM3 can be made for MM4, with the only difference that the sigma values for all corrections are a little bit bigger than before. But this was expected, since the protons are scattered at the readout-planes between MM3 and MM4. Please note, that the angles reconstructed for correction (1.) show the same values for MM3 and MM4.

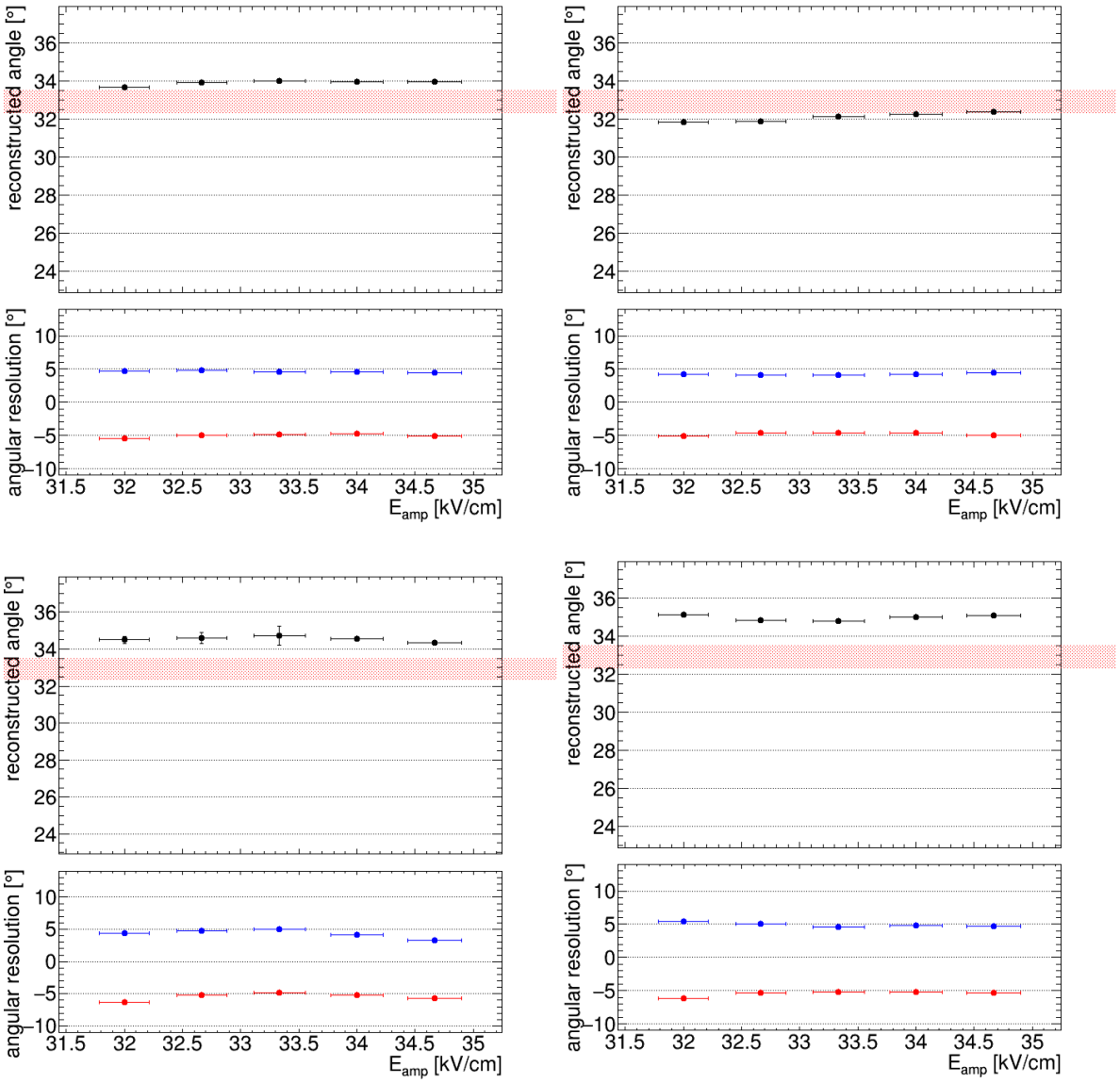

Figure 7.5: Angle of the beam axis and MM4 plotted for the different correction methods for standard FEC configuration. Common mode noise and baseline shift correction (top left), common mode noise correction by Bernhard Flierl (top right), baseline shift correction (bottom left), no correction (bottom right).

The reconstructed angle for MM3 is plotted versus the drift field for the different FEC configurations normal short and long in Fig. 7.7, here correction (1.) was applied. The reconstructed angles for the different configurations are almost the same showing only slight variations but differences can be seen in the sigma values. The biggest sigmas are for the standard configuration. The smallest are for the long configuration, as expected, because in chapter 6.1 it was shown that for the long configuration the most strips were hit. More strips enable a more precise determination of the cluster slope and therefore a more precise reconstruction of the angle.

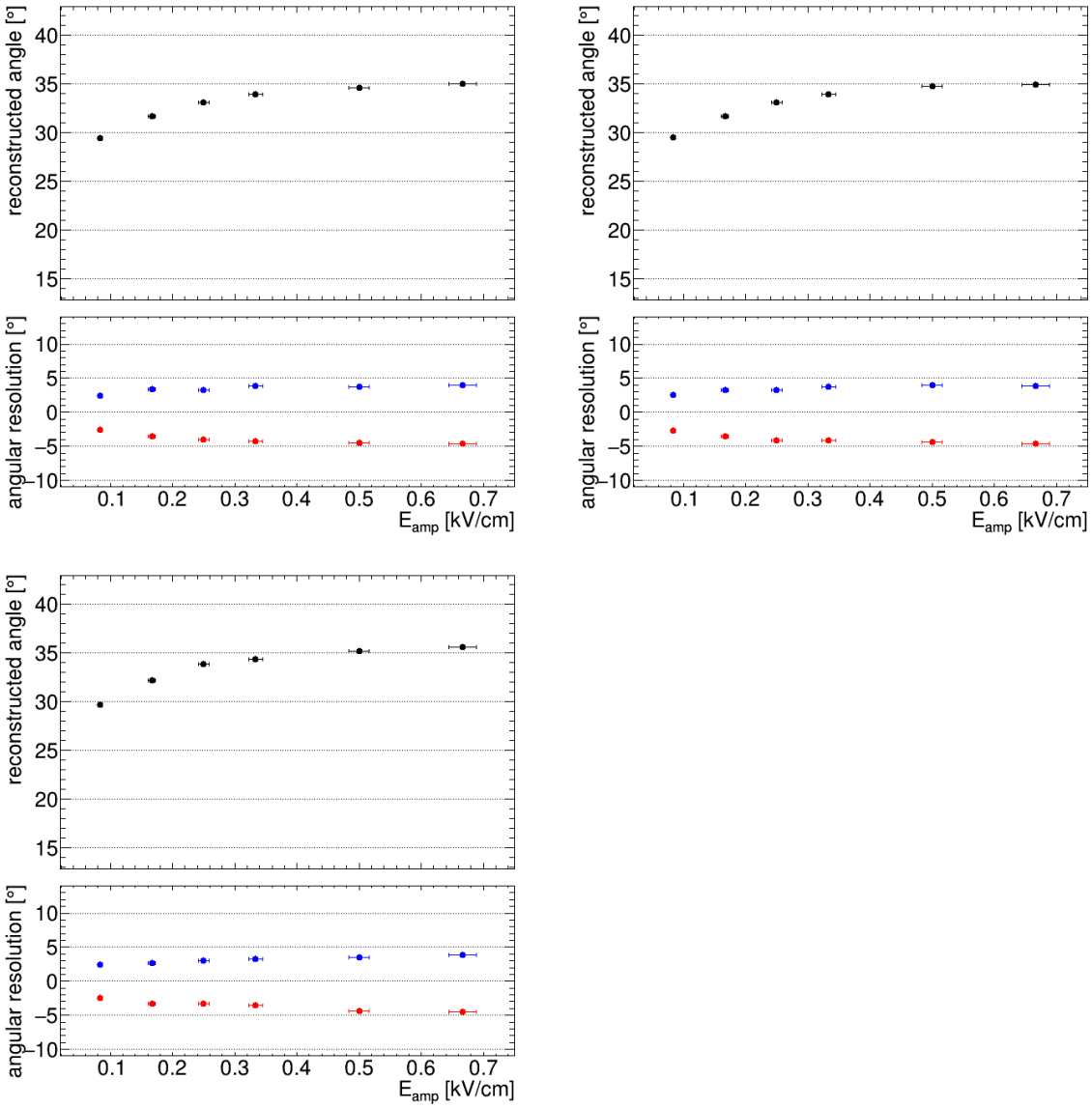

Figure 7.6: Reconstructed angle plotted versus the drift field for MM3 .

The comparison of the reconstructed angle for MM4 for the drift field scan cannot verify the observations made before. This may be due to the fact that the gaussian fit is limited to a certain range around the most probable value and and the fit range may be too narrow to confirm the observations made for MM3.

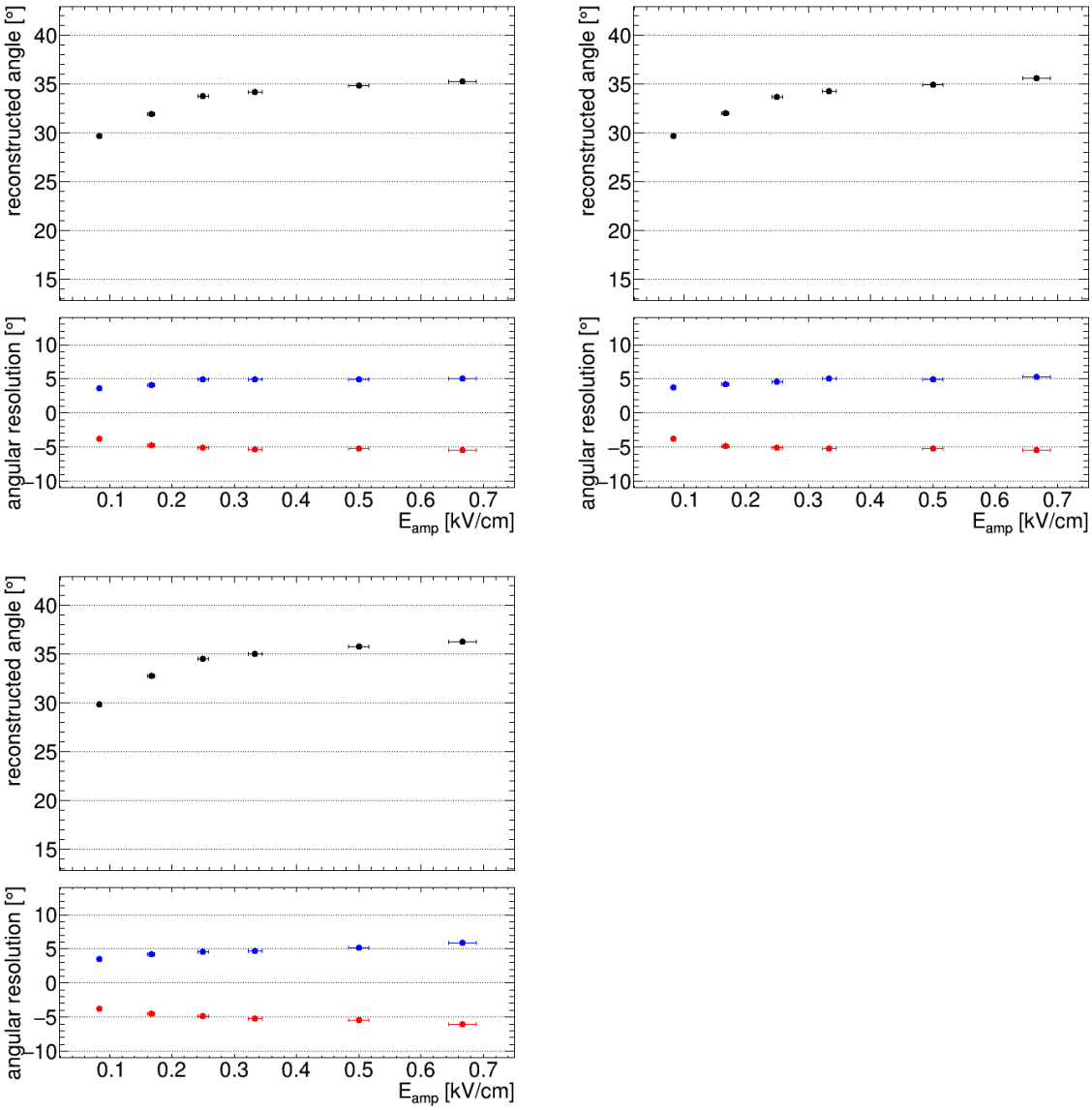

Figure 7.7: Angle of the beam axis and MM4 plotted for the different correction methods for standard FEC configuration. Common mode noise and baseline shift correction (top left), common mode noise correction by Bernhard Flierl (top right), baseline shift correction (bottom left), no correction (bottom right).

7.5 Conclusion

As shown in chapter 2.3, the electron velocity is highly dependent on the gas mixture, meaning that the used electron velocity contains a systematic error and therefore the difference in reconstructed angle and the expected angle should not be considered for comparison of the corrections.

The angular resolution was best improved by correction (1.), as it produced the most stable angle for a variation of the amplification field. This is especially important, since the slightest variations in the distance between micro-mesh and readout-plane can make huge differences in the amplification field strength. The results show high

statistics with more than 30000 events. As the statistics for correction (1.) were the lowest, the statistical uncertainties for this correction were the highest. Therefore, the variances of the distributions for the different corrections should be compared with caution.

The constant offset of the reconstructed angle can be eliminated via a calibration of the detector.

The other corrections did not show measureable improvements of angular resolution.

Chapter 8

Summary

For micromegas detectors in combination with the readout electronics used in the context of this thesis, three sources of signal distortion were identified:

- Common Mode Noise
- Baseline Shift
- False Sampling

A measurement of cosmic muons with a large micromegas chamber was realized at the Cosmic Ray Facility in Garching near Munich. With the acquired data, the properties of the baseline shift was studied in detail. A distance dependency of the baseline shift with respect to the center of gravity of the cluster could be shown and an advanced method for the calculation of the baseline shift at the center of the cluster was developed. The ratio between baseline shift and cluster charge was determined, enabling a powerful correction. Developed methods for the correction of the common mode noise and the false sampling were developed. A further measurement of protons was realized at the Tandem accelerator in Garching near Munich. A detector analysis of this setup was carried out identifying the detectors to use for the test of the corrections. The data were then corrected using the methods developed in this thesis. Then, the angle between the beam axis and the inclined detectors was reconstructed and compared for the different corrections and the uncorrected data. An improvement to angular resolution by the methods developed in the context of this thesis was shown.

8.1 Outlook

In the following, some possible further investigations which were not possible in the time frame of this thesis shall be discussed:

To verify if the baseline shift is an effect only caused by the APV, the baseline shift correction coefficients shall be determined for other experimental setups.

For the verification of the corrections, another experimental setup would be better suited, for example with a micromegas telescope placed in a 120 GeV pion beam at CERN. For such a setup, the highly energetic pions would not scatter as much as

the 20MeV protons of the Tandem beam, enabling precise particle tracking. The corrections can then be tested for an improvement of angular and spatial resolution.

8.2 Acknowledgements

I would like to thank all the people who supported me the last year:

I would like to thank my supervisor Philipp Lösel for his advice, support and comments.

I would like to thank Prof. Dr. Otmar Biebel for enabling this thesis, his good support and his fatherly advice.

I would also like to thank Ralf Müller, Andre Zibell, Bernhard Flierl, Felix Klitzner, Jona Bortfeldt and Ralf Hertenberger for all the discussions and the the good times we had.

I would also like to thank my family for making all this possible!

Bibliography

[1] Jona Bortfeldt. Floating Strip Micromegas Detector. *Dissertation (LMU Munich)*, 2013.

[2] ATLAS Collaboration. The atlas experiment at the cern large hadron collider. *JINST, 3*, 2008.

[3] Felix Klitzner. Investigating Floating Strip Micromegas Detectors and Development of a Large Area Micromegas Detector. *Master Thesis (LMU Munich)*, 2016.

[4] Joes Lawrence. APV25-S1 User Guide Version 2.2. 2001.

[5] C. Lefevre. Lhc: The guide (english version). 2008.

[6] Philipp Lösel. Performance Studies of Large Size Micromegas Detectors. *Master Thesis (LMU Munich)*, 2013.

[7] Magboltz. Magboltz cross sections. 2010.

[8] M.J. Berger R.M. Sternheimer and S.M. Seltzer. Density effect for the ionization loss of charged particles in various substances. atomic data and nuclear data tables, 30(2):261-271. 1984.

[9] J.P Robert Y. Giomataris, Ph. Reourgeard and G. Charpak. Micromegas: A high-granularity position sensitive gaseous detector for high particle-flux environments. nucl. instr. and meth. *Nucl. Instr. and Meth. A,376:29-35*, 1996.

[10] Andre Zibell. High-Rate Irradiation of 15mm Muon Drift Tubes and Development of an ATLAS Compatible Readout Driver for Micromegas Detectors. *Dissertation (LMU Munich)*, 2014.

Selbständigkeitserklärung

Ich versichere hiermit, die vorliegende Arbeit mit dem Titel

Studie von Vorverstärker-Schaltkreisen für Micromegas Detektoren

selbständig verfasst zu haben und keine anderen als die angegebenen Quellen und Hilfsmittel verwendet zu haben.

Quirin Steinbacher

München, den 6. Mai 2016